Fire Safety Journal 136 (2023) 103748

Contents lists available at ScienceDirect

Fire Safety Journal

journal homepage: www.elsevier.com/locate/firesaf

Stress–strain model for FRP confined heat-damaged concrete columns

Javad Shayanfar [a,*], Joaquim A.O. Barros [b], Mohammadali Rezazadeh [c]

[a] ISISE, Department of Civil Engineering, University of Minho, Azurém, 4800-058, Guimarães, Portugal
[b] ISISE, IBS, Department of Civil Engineering, University of Minho, Azurém, 4800-058, Guimarães, Portugal
[c] Civil Eng., Department of Mechanical and Construction Engineering, Northumbria University, Newcastle upon Tyne, NE1 8ST, United Kingdom

ARTICLE INFO

Keywords:
FRP confined heat-damaged concrete
Thermal damage
Confinement model
Dilation behavior

ABSTRACT

This paper is dedicated to the development of a new analysis-oriented model to simulate the axial and dilation behavior of FRP confined heat-damaged concrete columns under axial compressive loading. The model's calibration has considered the experimental results from concrete circular/square cross-section specimens submitted to a certain level of heat-induced damage, which after attained the environmental temperature, were fully confined with FRP jacket and tested. New equations were developed to determine the mechanical characteristics of unconfined heat-damaged concrete by performing regression analysis on a large database of experimental tests. Based on a parametric study on dilation behavior of FRP confined heat-damaged columns, a new dilation model was developed to predict concrete lateral strain at a given axial strain, dependent on the thermal damage level. By using this dilation model, a new methodology was introduced for predicting the axial stress-strain response of FRP confined heat-damaged columns in compliance with the active confinement approach. The adequate predictive performance of the model is demonstrated by estimating experimental axial stress-strain results.

1. introduction

During fire, concrete buildings generally demonstrate a better fire performance compared to timber and steel buildings due to concrete non-combustibility and relatively low thermal conductivity (Kodur [1], Bamonte and Lo Monte [2]). Nonetheless, depending on the fire intensity imposed to the structural elements, material deteriorations occur during fire exposure, resulting detrimental effects on the performance of concrete structures at their serviceability and ultimate limit state conditions (Demir et al. [3]). Considering the pre-existing thermal-induced damage, a post-fire strengthening solution for restoring its structural performance can be an environmental and economic sustainable solution over the demolishing and rebuilding alternative. To reinstate sufficiently axial responses of heat-damaged concrete columns (HC), externally bonded fiber-reinforced-polymer (FRP) composites have been demonstrated as a viable solution (Bisby et al. [4]).

Several experimental and analytical studies (i.e. Barros and Ferreira [5], Wang and Wu [6], Janwaen et al. [7], Shayanfar et al. [8]) were conducted to evaluate the capability of FRP confining strategy in upgrading the axial and dilation behavior of FRP confined concrete columns under axial compression at ambient conditions. For the case of FRP fully confined concrete columns of circular cross section at ambient conditions (FFCC-A, as shown in Fig. 1a), Barros and Ferreira [5] experimentally evidenced that the confinement-induced enhancements for normal-strength concrete is more pronounced than those registered in high-strength concrete. For the case of FRP fully confined concrete columns of square cross section at ambient conditions (FFSC-A, as shown in Fig. 1a), Wang and Wu [6] and Shan et al. [9] conducted experimental studies to evaluate the influence of cross-section circularity in the effectiveness of the confining strategy. It was evidenced that decreasing the corner radius (r) from $r = b/2$ (circular columns where b defines the length of the cross-section dimension) to $r = 0$ (square columns with sharp edges) results in a significant reduction in terms of confinement efficiency.

On the other hand, very limited experimental studies have been conducted for assessing the strengthening efficiency of FRP confining systems applied in the post-cooling regime of concrete specimens subjected to a certain maximum exposure temperature according to the heating scheme demonstrated in Fig. 1b. Bisby et al. [4] performed an experimental research to assess the effectiveness of FRP fully confinement on circular concrete columns subjected to different levels of maximum temperature (300, 500 and 700 °C) (FFCC–H, as shown in

* Corresponding author.
E-mail addresses: arch3d.ir@gmail.com (J. Shayanfar), barros@civil.uminho.pt (J.A.O. Barros), mohammadali.rezazadeh@northumbria.ac.uk (M. Rezazadeh).

https://doi.org/10.1016/j.firesaf.2023.103748
Received 11 March 2022; Received in revised form 4 October 2022; Accepted 19 January 2023
Available online 23 January 2023
0379-7112/© 2023 Elsevier Ltd. All rights reserved.

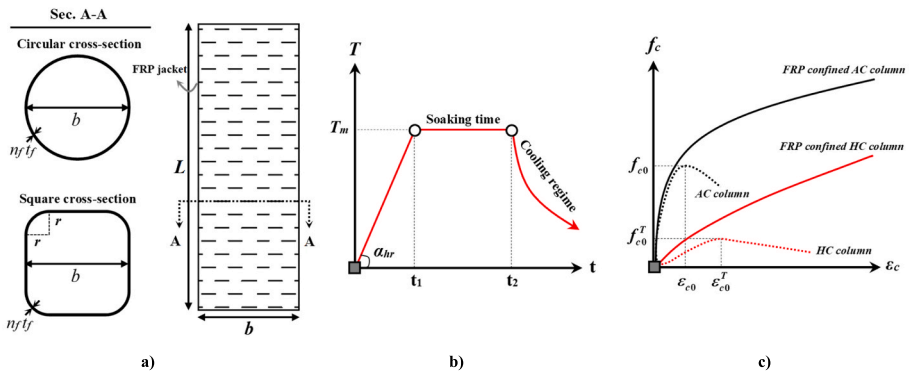

Fig. 1. a) Details of circular/square concrete columns with FRP full confinement; b) Typical temperature (T) versus time (t) curve as heating scheme; c) Typical Axial stress (f_c) versus axial strain (ε_c) curve. **Note:** T_m = maximum exposure temperature (target temperature); α_{hr} = heating rate; t_1 = time at which the temperature (T) reaches T_m; t_2 = time at which the heating process terminates; f_{c0} = peak compressive stress of unconfined concrete columns (AC) at ambient conditions; f_{c0}^T = peak compressive stress of unconfined heat-damaged concrete columns (HC); ε_{c0} = axial strain corresponding to f_{c0}; ε_{c0}^T = axial strain corresponding to f_{c0}^T; L = column's height; b = section dimension; r = corner radius; n_f = number of FRP layers; t_f = nominal FRP thickness.

Fig. 1a). It was evidenced that FRP confinement could significantly increase the axial compressive strength and stiffness of unconfined heat-damaged specimens (Fig. 1c). The peak axial compressive strength and the corresponding axial strain of FFCC-H specimens subjected to severe thermal exposure (700 °C) were almost 90% and 145%, respectively, of those of FFCC at ambient conditions. However, the secant axial stiffness of FFCC-H specimens (as the ratio of axial stress to its corresponding axial strain) was reported to be considerably lower than that of FFCC, and this difference has increased with maximum exposure temperature (T_m). Lenwari et al. [10] experimentally evidenced that the axial stress versus axial strain response of FFCC-H is dependent on the used heating scheme, i.e. T_m, exposure duration and cooling regime (air or water cooling methods), and on the axial compressive strength of AC, which was also confirmed by Luo et al. [11]. Furthermore, it was shown that the level of axial strength improvements, induced by FRP confining system, is higher in HC than in AC. Accordingly, for HC with a high level of thermal damage, FRP effectiveness tends to be more significant. Ouyang et al. [12] investigated experimentally the dilation behavior of heat-damaged circular concrete specimens confined by Basalt FRP (BFRP) jacket (FFCC–H) under axial compressive loading. It was demonstrated that there is a noticeable difference between the transverse expansibility of HC subjected to different level of the imposed T_m. Furthermore, the recorded hoop strains at BFRP rupture were almost independent of the exposure temperature. Song et al. [13] experimentally evidenced the high potential of BFRP confining system for improving the axial and dilation responses of HC with square cross-section (FFSC–H, as shown in Fig. 1a). The confinement-induced enhancements were more pronounced in HC exposed to high temperatures and confined by thicker BFRP jackets.

For the prediction of the axial stress-strain response of FRP confined AC columns, several analysis-oriented models, based on active confinement approach, have been recommended i.e. Teng et al. [14], Lim and Ozbakkaloglu [15], and Shayanfar et al. [16and17]. Teng et al. [14] proposed an analysis-oriented model for passively confined concrete, whose calibration was based on experimental observations in FRP fully confined concrete specimens of circular cross section (FFCC). Based on theoretical principles and experimental evidences, Shayanfar et al. [16] developed a generalized analysis-oriented model for passive confinement arrangements, whose parameters were derived from the experimental results with FRP fully/partially confined circular concrete specimens. Shayanfar et al. [17] extended Shayanfar et al. [16]'s model to make it applicable to the case of columns of square-cross section, by simulating the influence of the non-circularity in terms of confinement-induced enhancements. Bisby et al. [4] proposed a design-oriented model to determine the axial response of heat-damaged circular cross-section concrete columns confined by FRP (FFCC–H). In this model, the confinement-induced improvements were expressed as a main function of maximum exposure temperature (T_m) imposed to the column. Nevertheless, an analysis-oriented model to simulate the full-range of dilation and axial responses of FRP fully confined HC columns with square cross-section is still lacking.

This paper aims to introduce a new methodology to determine the axial stress-strain response of FRP fully confined circular/square HC columns (the concrete specimens were submitted to a certain T_m, and after having attained the environmental temperature, the fully confining FRP jacket was applied to the heat-damaged concrete). For the case of unconfined heat-damaged concrete, through regression analysis performed on a large test database, new expressions are developed to determine its mechanical characteristics in terms of axial compressive strength and its corresponding axial strain. By performing parametric studies with the available experimental data, the significant influence of the pre-existing thermal-induced damage on the establishment of the axial and dilation behavior of FRP fully confined heat-damaged concrete columns is demonstrated. By performing a parametric study to assess the influence of T_m on the concrete transverse expansion, a new dilation model depending on the heat-damaged level is proposed, which has a unified character with the dilation model developed by Shayanfar et al. [17] for concrete specimens at room temperature. By using the developed dilation model, a new methodology is introduced, based on active confinement approach, for the simulation of the axial stress-strain response of FRP fully confined circular/square HC columns at the different levels of T_m. The model's adequate predictive performance is demonstrated by estimating experimental axial stress-strain responses.

2. Unconfined heat-damaged concrete columns (HC)

Kodur [1] evidenced that post-fire response of HC columns significantly depends on concrete mechanical, thermal (including thermal conductivity, thermal diffusivity, specific heat, and mass loss) and deformation (including concrete thermal expansion) properties, as well as on the spalling response. In general, concrete submitted to maximum exposure temperature (T_m) up to 100 °C can be considered almost undamaged. Afterward, water loss (causing shrinkage) and the expansion of aggregates induce internal stresses in the concrete, particularly for $T_m \geq 300$°C. Furthermore, thermal-induced chemical processes and thermo-mechanical damages lead to a significant strength degradation for the concrete submitted to high levels of exposure temperature [1]. A comprehensive review of concrete properties at elevated temperatures can be found in Kodur and Sultan [18], Hertz [19], Raut and Kodur [20], Aslani and Bastami [21].

In terms of mechanical properties, by submitting concrete to elevated temperature with a heating scheme including maximum exposure temperature (T_m), the axial compressive stress of HC (f_c^T) and the modulus of elasticity (E_{cT}) decrease depending upon its peak axial strength (f_{c0}^T). However, axial strains corresponding to the peak (ε_{c0}^T) and ultimate stages (ε_{cu0}^T) increase, demonstrating a significant reduction on the axial stiffness (defined as f_c^T/ε_c where ε_c is the axial strain) of HC compared to AC (Hertz [19], Chang et al. [22], Al-Salloum et al. [23], Sharma et al. [24], Geng et al. [25], Xiao et al. [26], Xiang et al. [27]).

Table 1
Summary of experimental results in the assembled database.

Number of datasets		f_{c0} range (MPa)	f_{c0}^{T} range (MPa)	T_m range (° C)	b range (mm)
292	**Min.**	16.1	3.8	100	71
	Max.	136.3	107.4	800	170
	Mean	56.0	29.6	514	129.5
	CoV	0.446	0.636	0.408	0.225

2.1. Peak axial strength of HC (f_{c0}^{T})

Experimental studies evidenced that the heat-induced damages in HC columns lead to a reduction in terms of peak axial strength. Accordingly, by defining the axial strength ratio, β_{0T}, (the ratio of f_{c0}^{T} and f_{c0}), f_{c0}^{T} can be expressed as:

$$f_{c0}^{T} = \beta_{0T} f_{c0} \tag{1}$$

The variation of $\beta_{0T}{}^{Exp} = f_{c0}^{T\,Exp}/f_{c0}{}^{Exp}$ with respect to T_m can be obtained from experimental results of axial compression tests on HC

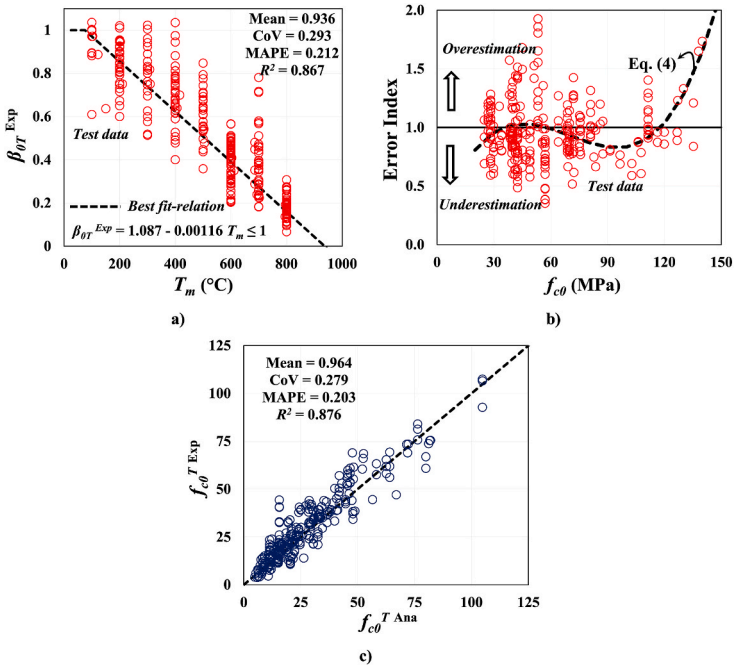

Fig. 2. a) Variation of $f_{c0}^{T\,Exp}$ as a function of T_m; b) predictive performance of Eq. (1).

Table 2
Performance of different models for predicting f_{c0}^{T}, by using the assembled database information.

Model	Expression	Test Data	Assessment indicators		
			Mean	CoV	MAPE
Proposed model	$f_{c0}^{T} = (1.087 - 0.00116T_m)\frac{f_{c0}}{\gamma_f} \le f_{c0}$	**292**	**0.964**	**0.279**	**0.203**
Li and Purkiss [28]	$f_{c0}^{T} = \left(0.00165\left(\frac{T_m}{100}\right)^3 - 0.03\left(\frac{T_m}{100}\right)^2 + 0.025\left(\frac{T_m}{100}\right) + 1.002\right) f_{c0}$	292	0.986	0.304	0.220
Chang et al. [22]	$f_{c0}^{T} = \begin{cases} (1.01 - 0.00055T_m)f_{c0} & 20^{\circ}C \le T_m \le 200^{\circ}C \\ (1.15 - 0.00125T_m)f_{c0} & 200^{\circ}C \le T_m \le 800^{\circ}C \end{cases}$	292	0.951	0.291	0.210
Hertz [19]	$f_{c0}^{T} = \frac{f_{c0}}{1 + \frac{T_m}{T_1} + \left(\frac{T_m}{T_2}\right)^2 + \left(\frac{T_m}{T_8}\right)^8 + \left(\frac{T_m}{T_{64}}\right)^{64}}$ in which $T_1 = 15000^{\circ}C$, $T_2 = 800^{\circ}C$, $T_8 = 570^{\circ}C$ and $T_{64} = 100000^{\circ}C$ for the case of siliceous aggregate; $T_1 = 100000^{\circ}C$, $T_2 = 1100^{\circ}C$, $T_8 = 800^{\circ}C$ and $T_{64} = 940^{\circ}C$ for the case of lightweight aggregate; $T_1 = 100000^{\circ}C$, $T_2 = 1080^{\circ}C$, $T_8 = 690^{\circ}C$ and $T_{64} = 1000^{\circ}C$ for the case of other types of aggregates.	292	1.283	0.323	0.335
Han and Huo [29]	$f_{c0}^{T} = \frac{f_{c0}}{1 + 2.4(T_m - 20)^6 \times 10^{-17}}$	292	1.168	0.318	0.295
Eurocode [30]	$f_{c0}^{T} = \begin{cases} f_{c0} & T_m \le 100^{\circ}C \\ (1.067 - 0.00067T_m)f_{c0} & 100^{\circ}C \le T_m \le 400^{\circ}C \\ (1.44 - 0.0016T_m)f_{c0} & T_m \ge 400^{\circ}C \end{cases}$	292	1.089	0.296	0.227
Lie et al. [31]	$f_{c0}^{T} = \begin{cases} (1 - 0.001T_m)f_{c0} & T_m \le 500^{\circ}C \\ (1.375 - 0.00175T_m)f_{c0} & 500^{\circ}C \le T_m \le 700^{\circ}C \\ 0 & T_m \ge 700^{\circ}C \end{cases}$	292	0.678	0.546	0.374
Lie and Lin [32]	$f_{c0}^{T} = \left(2.011 - 2.353\frac{T_m - 20}{1000}\right) f_{c0} \le f_{c0}$	292	1.340	0.332	0.400

Table 3
Summary of experimental results in the assemble database.

Number of datasets		f_{c0} range (MPa)	ε_{c0} range	λ_L range	d_{eq} range (mm)
604	Min.	11.6	0.0012	1.0	54
	Max.	204.0	0.0051	5.5	500
	Mean	51.2	0.0025	2.2	133.4
	CoV	0.534	0.233	0.297	0.339

columns. In the present study, a database of 292 HC column specimens with a wide range of concrete properties and exposure temperature was collected, as briefly presented in Table 1. The following criteria were adopted to include/exclude experimental data: 1) ones obtained from circular/square/rectangular heat-damaged concrete specimens tested under concentric were included; 2) heat-damaged concrete specimens subjected to a maximum exposure temperature more than 800 °C were excluded; 3) light-weight concrete specimens were excluded; 4) light-weight concrete, and recycled aggregate concrete specimens were excluded; 5) data registered experimentally with incomplete documented information, i.e. maximum exposure temperature, geometry details and material properties, were excluded.

Fig. 2a shows the variation of ${\beta_{0T}}^{Exp}$ with respect to T_m, based on the results of the database, where a decrease of ${\beta_{0T}}^{Exp}$ with the increase of T_m, from 1 to almost 0.2 corresponding to room conditions and 800 °C, respectively, is visible. Based on the best-fit relation obtained from regression analysis on the database information, β_{0T} versus T_m data can be obtained as $\beta_{0T} = 1.087 - 0.00116T_m$. By assuming *Error Index* as $(1.087 - 0.00116T_m)/{\beta_{0T}}^{Exp}$, Fig. 2b demonstrates that there is a slight variation in Error Index versus concrete strength relationship which is less than one up to almost $f_{c0} = 110$ MPa, representing underestimation. However, beyond $f_{c0} = 110$ MPa, the Error Index tend to be more than 1 resulting in overestimation of the experimental counterparts. Accordingly, based on regression analysis performed on the Error Index and concrete strength relationship, β_{0T} can be calculated by:

$$\beta_{0T} = \frac{1.087 - 0.00116T_m}{\gamma_f} \leq 1 \tag{2}$$

in which

$$\gamma_f = 1 + (\gamma_0 - 1)\left(\frac{T_m - 25}{100}\right) \quad \text{for } T_m \leq 100°C \tag{3a}$$

$$\gamma_f = \gamma_0 \quad \text{for } T_m \geq 100°C \tag{3b}$$

$$\gamma_0 = 3415\left(\frac{f_{c0}}{1000}\right)^3 - 721\left(\frac{f_{c0}}{1000}\right)^2 + 44.5\left(\frac{f_{c0}}{1000}\right) + 0.178 \tag{4}$$

where the developed expression is valid for $T_m \leq 800°C$ based on the interval of the submitted maximum exposure temperatures ($T_m = [25°C, 800\ °C]$) in the database used for the regression analysis. γ_0 reflects the influence of f_{c0} (in MPa) in the determination of β_{0T} empirically.

In Fig. 2c, the results predicted by the proposed model are compared to those reported by the experiments (Table 2), with a mean = 0.964, a coefficient of variation (CoV) = 0.279, a mean absolute percentage error (MAPE) = 0.203, and an R-squared value (R^2) = 0.876, revealing an acceptable predictive performance. Table 2 also shows that the proposed model provides a predictive performance better than of the existing models.

2.2. Axial strain at the peak stage of AC columns (ε_{c0})

For the case of AC columns, the experimental and analytical studies conducted by Refs. [33–38] evidenced that ε_{c0} increases with the concrete compressive strength (f_{c0}). Jansen and Shah [34] experimentally demonstrated that the column aspect ratio (λ_L as the ratio of the column height to its diameter) has also considerable influence on ε_{c0} due to the occurrence of strain-localization within a finite zone with a pronounced gradient of deformations due to the concrete post-peak strain-softening behavior. In this study, in order to estimate ε_{c0}, a large database (Table 3) was compiled from the experimental results available in the literature, resulting in 604 unconfined concrete specimens (AC) with a broad range of concrete properties and geometry configurations. Note that for the case of non-circular columns with a total cross-section area of A_g, based on Yang et al. [38] recommendations, λ_L can be determined as L/d_{eq} where L is the columns' height and d_{eq} is the equivalent circular diameter ($d_{eq} = \sqrt{4A_g/\pi}$ [38]).

Based on a preliminary sensitivity analysis, a low effect was achieved for the influence of the column size (i.e. the normalized $d_{eq}/150$, with d_{eq} in mm) to estimate ε_{c0} when compared to other influencing factors (f_{c0} and λ_L). Accordingly, using regression analysis, the best-fit expression to predict ε_{c0} was derived as a function of f_{c0} and λ_L regardless of the column's cross-section dimension influence:

$$\varepsilon_{c0} = 0.0011\left(\frac{f_{c0}}{\lambda_L}\right)^{0.25} \tag{5}$$

Table 4 evaluates the predictive performance of this relation with the results of the experimental tests, and also compares with that of existing models. Based on the assessment indicators (values of mean = 0.977, CoV = 0.184 and MAPE = 0.138), there is an acceptable agreement between model prediction and the experimental results. Furthermore, compared to the models recommended by Popovics [39], Karthik and Mander [40] and Lim and Ozbakkaloglu [41], it is the most accurate one, confirming its reliability.

2.3. Axial strain at the peak stage of HC columns (ε_{c0}^T)

The experiments with HC columns conducted by Chang et al. [22], Sharma et al. [24], Xiao et al. [26], Xiang et al. [27] evidenced that the axial strain (ε_{c0}^T) corresponding to f_{c0}^T tends to increase significantly from ε_{c0} at ambient condition to $\varepsilon_{c0}^T \gg \varepsilon_{c0}$ at elevated temperature, as shown in Fig. 3a.

The details of the experimental specimens in the assembled database, including 225 tested HC columns, is presented in Table 5.

The best-fit relation between ${\varepsilon_{c0}^T}^{Exp}/\varepsilon_{c0} - 1$ (representing the thermal damage-induced strain) and T_m was obtained from regression analysis by considering the influence of f_{c0}, resulting:

$$\varepsilon_{c0}^T = \left(1 + 63{f_{c0}}^{-0.5}\left(\frac{T_m}{1000}\right)^{4.2}\right)\frac{\varepsilon_{c0}}{\alpha_T} \leq 4.5\frac{\varepsilon_{c0}}{\alpha_T} \tag{6}$$

Table 4
Performance of different models for predicting ε_{c0}, by using the assembled database.

Model	Expression	Test Data	Assessment indicators		
			Mean	CoV	MAPE
Proposed model	$\varepsilon_{c0} = 0.0011(f_{c0}/\lambda_L)^{0.25}$	604	**0.977**	**0.184**	**0.138**
Lim and Ozbakkaloglu [41]	$\varepsilon_{c0} = 0.001{f_{c0}}^{0.225}(152/D)^{0.1}(2/\lambda_L)^{0.13}$	**604**	0.988	0.188	0.143
Karthik and Mander [40]	$\varepsilon_{c0} = 0.0015 + f_{c0}/70000$	604	0.915	0.204	0.153
Popovics [39]	$\varepsilon_{c0} = 0.000937{f_{c0}}^{0.25}$	604	1.009	0.190	0.147

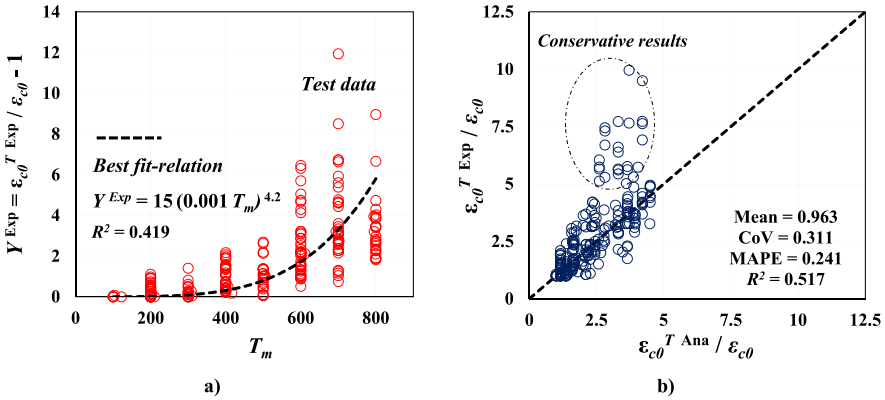

Fig. 3. a) Variation of $\varepsilon_{c0}^{T\ Exp}$ with the temperature T; b) Predictive performance of Eq. (6).

Table 5
Details of the experimental results in the assembled database.

Number of datasets		f_{c0}^{T} range (MPa)	ε_{c0}^{T} range	T_m range (°C)	d_{eq} range (mm)
225	Min.	25.0	0.0013	100	80
	Max.	111.4	0.0260	800	169
	Mean	53.3	0.0064	502	135
	CoV	0.398	0.653	0.409	0.181

in which

$$\alpha_T = 1 \quad \text{for } T_m \le 100^{\circ}\text{C} \tag{7a}$$

$$\alpha_T = 1.22 - 0.0025T_m + 3\times10^{-6}T_m{}^2 \quad \text{for } T_m > 100^{\circ}\text{C} \tag{7b}$$

where the developed expression is valid for $T_m \le 800^{\circ}$C based on the interval of the submitted maximum exposure temperatures (T_m = [25°C, 800 °C]) in the database used for the regression analysis. α_T is the calibration factor for the influence of T_m in the increase of axial strain induced by thermal damage, obtained from the regression analysis. In Fig. 3b and Table 6, the predictive performance of this model is assessed based on 225 test specimen results. As can be seen, Eq. (6) provides the most accurate model compared to the existing models in the prediction of the experimental counterparts, even though conservative results were achieved for some cases submitted to high level of exposure temperature.

3. Dilation behavior of FRP confined HC columns

3.1. Confinement pressure developed for ambient condition

For the case of FRP fully confined square AC columns (FFSC), based on the force equilibrium at the cross-sectional level, confinement pressure ($f_{l,f}$) generated by the FRP confining stress (f_f) can be expressed as (Shayanfar et al. [17]):

$$f_{l,f} = 2K_e\frac{n_f t_f}{D_{eq}}f_f \tag{8}$$

where n_f is the number of FRP layers; and t_f is the nominal thickness of one FRP layer. In Eq. (8), D_{eq} defines the diameter of the equivalent circular cross-section for columns of square cross section with b edge and r corner radius, which can be calculated as recommended by Shayanfar et al. [17]:

$$D_{eq} = \frac{1-0.215R_b{}^2}{1-0.215R_b}b \tag{9a}$$

where

$$R_b = 2r/b \tag{9b}$$

is the corner radius ratio. Note that by using D_{eq} in the determination of FRP confinement pressure, FRP volumetric ratio in the equivalent circular cross-section would be identical to that of original square cross-section column. In Eq. (8), K_e is the confinement efficiency factor. Shayanfar et al. [17] modified the original concept of '*confinement efficiency factor*' by considering the impact of concrete expansion gradient in the establishment of confinement pressure, besides the well-known phenomenon of arching action. By using this concept, the actual

Table 6
Performance of different models for predicting ε_{c0}^{T}, by using the assembled database.

Model	Expression	Test Data	Assessment indicators		
			Mean	CoV	MAPE
Proposed model	$\varepsilon_{c0}^{T} = \left(1 + 63f_{c0}{}^{-0.5}\left(\frac{T_m}{1000}\right)^{4.2}\right)\frac{\varepsilon_{c0}}{\alpha_T}$	**225**	**0.963**	**0.323**	**0.241**
Chang et al. [22]	$\varepsilon_{c0}^{T} = \left[(7.7-0.1f_{c0})\left(\frac{e^{0.01\times T_m-5.8}}{e^{0.01\times T_m-5.8}+1}-0.0219\right)+1\right]\varepsilon_{c0} \ge \varepsilon_{c0}$	**225**	0.805	0.453	0.337
Li and Purkiss [28]	$\varepsilon_{c0}^{T} = \frac{2f_{c0}}{E_c}+0.21\times10^{-4}(T_m-20)-0.9\times10^{-8}(T_m-20)^2$	**225**	**2.120**	0.418	**1.150**
Terro [42]	$\varepsilon_{c0}^{T} = (0.9615+0.0019T_m)\varepsilon_{c0}$	**225**	0.888	0.446	0.348
Khennane and Baker [43]	$\varepsilon_{c0}^{T} = \begin{cases} 0.003 & 20^{\circ}\text{C} \le T_m \le 200\ ^{\circ}\text{C} \\ 0.000686+0.00001156T_m \le 0.0082 & T_m \ge 200^{\circ}\text{C} \end{cases}$	**225**	1.193	0.402	0.379
Bazant and Chern [44]	$\varepsilon_{c0}^{T} = \begin{cases} 0.00216+0.0000064\,T_m & 20^{\circ}\text{C} \le T_m \le 600\ ^{\circ}\text{C} \\ 0.003+0.000015\,T_m & 600 \le T_m{}^{\circ}\text{C} \end{cases}$	**225**	1.460	0.362	0.538
Lie [45]	$\varepsilon_{c0}^{T} = 0.0025+(6T_m+0.04T_m{}^2)10^{-6}$	**225**	2.929	0.381	1.929

confinement pressure acting non-homogenously on the concrete is converted to an equivalent confinement pressure with uniform distribution along transverse and longitudinal directions of the column. This factor includes two components, which can be determined as suggested by Shayanfar et al. [17]:

$$K_e = K_H K_V \tag{10}$$

where K_H is the horizontal component, reflecting the influence of horizontal arching action on the distribution of confinement pressure within the cross-section of a non-circular columns (for circular columns, $K_H = 1$), determined as:

$$K_H = R_b \geq 0.07 \tag{11}$$

In Eq. (10), K_V is the vertical component reflecting the influence of the gradient of concrete lateral expansion along the column height, depending on the level of confinement stiffness (the ratio of confinement pressure to concrete lateral strain). It was demonstrated by Shayanfar et al. [16] that above a certain level of confinement stiffness, the confinement imposed to the concrete is strong enough to strictly control the evolution of concrete expansion leading to an almost null gradient along the vertical direction ($K_V = 1$). However, for the cases with an insufficient confinement stiffness, due to the lack of strong restriction in the curtailment of concrete expansibility, the concrete column is expected to experience a highly non-homogenous distribution of concrete expansion and, consequently, the confinement pressure in the axial loading direction is non-uniform. Shayanfar et al. [17] suggested a design-based formulation to calculate K_V as follows:

$$K_V = \frac{1}{3} + \frac{2}{3} k_\varepsilon \tag{12}$$

in which

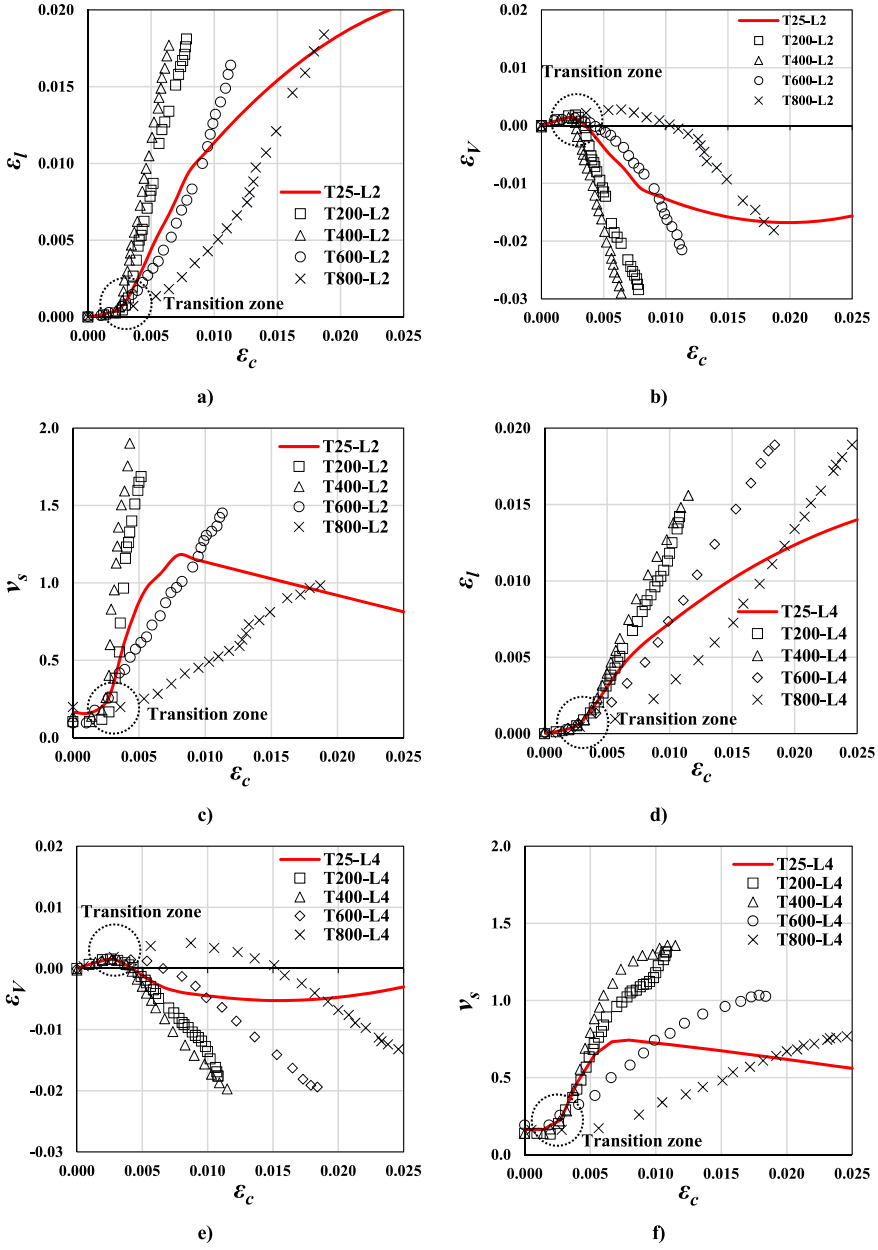

Fig. 4. Evaluation of dilation behavior of BFRP confined HC columns with two layers: a) ε_l versus ε_c; b) ε_V versus ε_c; c) ν_s versus ε_c; and four layers d) ε_l versus ε_c; e) ε_V versus ε_c; f) ν_s versus ε_c.
Note: The results related to T25-L2 and T25-L4 were determined based on the dilation model developed by Shayanfar et al. [8and17].

$$k_\varepsilon = 0.08 + 0.92\left[2\frac{I_f}{I_f^*} - \left(\frac{I_f}{I_f^*}\right)^2\right] \le 1 \quad \text{for } I_f \le I_f^* \tag{13a}$$

$$k_\varepsilon = 1 \quad \text{for } I_f > I_f^* \tag{13b}$$

$$I_f^* = 0.06 + 0.0005 f_{c0} \tag{14}$$

$$I_f = 2K_H \frac{n_f t_f E_f \varepsilon_{c0}}{D_{eq} f_{c0}} \simeq K_H \frac{n_f t_f E_f}{550 D_{eq} {f_{c0}}^{0.75}} \tag{15}$$

where k_ε represents the ratio of minimum and maximum concrete lateral expansion along the column height. I_f represents the confinement stiffness index regardless the influence of the gradient of concrete expansion along the column height. Finally, I_f^* is the confinement stiffness index above which $K_V = 1$, representing the homogenous concrete expansion along the column due to strong restrictions imposed to the concrete.

In this paper, for further simplification of the relative complexity of Eqs. 12–15 in the calculation of K_V, a simplified equation was developed based on a preliminary sensitivity analysis on the influencing factors in Eq. (12) as:

$$K_V = 2.2\left(I_f\right)^{0.3} \le 1 \tag{16}$$

Accordingly, by using the design-based Eqs. (11), (15) and (16), the two components involved in K_e (Eq. (10)) can be calculated.

3.2. Confinement pressure developed for elevated condition

Based on the model developed for ambient conditions in the previous section, the confinement pressure (f_{lf}^T) imposed by the FRP confining stress (f_f) to HC column can be expressed as:

$$f_{lf}^T = 2K_e^T \frac{n_f t_f}{D_{eq}} f_f^T \tag{17}$$

in which

$$K_e^T = K_H K_V^T \tag{18}$$

where K_H can be determined by Eq. (11). Through the substitution of confinement stiffness index of FRP confined HC columns (I_f^T) with that of FRP confined AC ones (I_f) in Eq. (16), K_V^T can be expressed as:

$$K_V^T = 2.2\left(I_f^T\right)^{0.3} = 2.2{\beta_{0T}}^{-0.45}\left(I_f\right)^{0.3} \le 1 \tag{19}$$

in which based on Eq. (15),

$$I_f^T = K_H \frac{n_f t_f E_f}{550 D_{eq}\left(f_{c0}^T\right)^{0.75}} = {\beta_{0T}}^{-0.75} I_f \tag{20}$$

where β_{0T} is the axial strength ratio calculated by Eq. (2), which is equal to 1 for concrete at ambient condition; Considering that f_f^T can be calculated as $E_f \varepsilon_h^T = E_f \varepsilon_l^T$ (where ε_h^T and ε_l^T are the generated circumferential (hoop) and radial strains, respectively, and E_f is the FRP modulus elasticity), Eq. (17) is rearranged as:

$$f_{lf}^T = 2K_e^T \frac{n_f t_f}{D_{eq}} E_f {\varepsilon_h}^T \tag{21}$$

Based on Poisson's ratio effect ($\varepsilon_h^T = \varepsilon_l^T = \nu_s^T \varepsilon_c$, where ν_s^T is the secant Poisson's ratio), Eq. (21) can be rearranged as:

$$f_{lf}{}^T = 2K_e \frac{n_f t_f}{D_{eq}} E_f {\nu_s}^T \varepsilon_c \tag{22}$$

Accordingly, in order to calculate f_{lf}^T imposed to the concrete at a certain level of ε_c, the corresponding ν_s^T is required to be addressed, which will be presented in the following section.

3.3. Dilation mechanism at elevated conditions

During axial compressive loading, after splitting cracks have occurred, by increasing the axial strain, the development of concrete lateral expansion abruptly increases due to Poisson's ratio effect. Experimental studies conducted by Barros and Ferreira [5], Mirmiran and Shahawy [46], Lim and Ozbakkaloglu [47] and Zeng et al. [48] evidenced that the magnitude of concrete dilatancy is strongly dependent on confinement stiffness imposed to the concrete. For the case of AC with a high level of confinement stiffness capable of limiting the evolution of concrete expansion and splitting cracks, a remarkable enhancement in terms of axial strength and deformability is obtained (Barros and Ferreira [5]). However, for the case of low confinement stiffness, the confinement pressure imposed to the concrete is not able to overcome the concrete tendency for abrupt expansion, leading to lower confinement-induced enhancements [49].

For a preliminary assessment of the dilation response of FRP confined HC columns, the experimental dilation results conducted by Ouyang et al. [12] are analyzed. All tests were conducted with specimens of diameter and height of 150 mm and 300 mm, respectively. The unconfined concrete compressive strength at the ambient condition was reported 45.1 MPa. Basalt FRP (BFRP) was used with the values of thickness, modulus of elasticity and rupture strain of 0.121 mm, 108.3 GPa and 2.18%, respectively. The HC columns were subjected initially to various levels of maximum temperature (200 °C, 400 °C, 600 °C and 800 °C). Then, they were fully confined with two and four layers of BFRP. Fig. 4 demonstrates the experimental dilation responses of BFRP confined HC specimens reported by Ouyang et al. [12]. Here, ε_V is the volumetric strain determined as $\varepsilon_V = \varepsilon_c - 2\varepsilon_l = (1 - 2\nu_s)\varepsilon_c$ in which ν_s is the secant Poisson's ratio as $\nu_s = \varepsilon_l/\varepsilon_c$. Moreover, the negative and positive values of ε_V represent volumetric expansion and contraction, respectively. To better demonstrate the contribution of thermal-induced damage level in terms of dilation behavior, the model developed by Shayanfar et al. [8and17] was followed to determine the dilation results associated with FRP confined AC specimens (***T25-L2*** and ***T25-L4*** with red solid lines). Note that Ti-Lj refers to the concrete column heated up to the i-th maximum exposure temperature (Ti) and then, confined by j layers of BFRP.

As can be seen in Fig. 4, for all cases, regardless the level of thermal-induced damage, initial behavior up to transition zone is virtually the same. However, beyond the transition zone, there is a noticeable difference between the transverse expansibility of HC and AC specimens. Fig. 4a reveals that at a certain axial strain (ε_c), lateral strain (ε_l) for the cases of T200-L2 and T400-L2 was obtained significantly higher than that of T25-L2, demonstrating the effect of thermal damage on increase of ε_l. Likewise, from Fig. 4b, T200-L2 and T400-L2 have experienced a large incremental volumetric expansion. However, in the T25-L2, beyond $\varepsilon_c = 0.008$, a considerable decrease in the magnitude of the increase in volumetric strain (ε_v) with respect to ε_c, followed by a reverse in volumetric evolution around $\varepsilon_c = 0.02$, reveals the capability of the confinement system imposed to AC column (T25-L2) in limiting the transverse expansibility of AC columns. Likewise, as demonstrated in Fig. 4c, for T25-L2, due to the adequate activated confinement imposed to AC column to overcome its tendency for lateral expansibility, beyond the peak stage, ν_s trend followed a decreasing branch. Even though, heat-induced expansion for HC columns leads to an earlier activation in passive confining system of T200-L2 and T400-L2, the applied confinement was not adequate to strongly constrain the concrete expansion evolution, based on its abrupt increase in ν_s after transition zone. On the other hand, for the cases subjected to high level of temperature (T600-L2 and T800-L2), as shown in Fig. 4a, at a certain level of ε_l, T600-L2 and T800-L2 experienced a larger axial deformation depending on thermal damage level, compared to T25-L2, T200-L2 and T400-L2. Likewise, Fig. 4b reveals that up to a certain level of axial strain, the changes in volumetric evolution for T600-L2 and T800-L2 were almost marginal, while they underwent large axial deformations.

Table 7
Database of the axial compressive tests on heat-damaged concrete confined by FRP jacket.

Reference ID		Influential parameters								Experimental and analytical results					
		b (mm)	R_b	f_{c0} (MPa)	T_m (°C)	$\eta_f \times t_f$ (mm)	E_f (GPa)	ε_{fu}	$\rho_{k,f}$	$\eta_{T\ Exp}$	$\eta_{T\ Ana}$	$\frac{\eta_T^{Ana}}{\eta_T^{Exp}}$	$v_{s,max}^{T\ Exp}$	$v_{s,max}^{T\ Ana}$	$\frac{v_{s,max}^{T\ Ana}}{v_{s,max}^{T\ Exp}}$
Ouyang *et al.* [12]	**T800-L2-1**	150	1.0	45.1	800	0.242	108	0.022	0.012	0.83	0.83	**1.00**	0.98	0.98	**1.00**
	T800-L2-2	150	1.0	45.1	800	0.242	108	0.022	0.012	0.86	0.83	**0.96**	1.02	0.98	**0.96**
	T800-L2-3	150	1.0	45.1	800	0.242	108	0.022	0.012	0.74	0.83	**1.12**	0.88	0.98	**1.12**
	T600-L2-1	150	1.0	45.1	600	0.242	108	0.022	0.012	1.23	1.04	**0.85**	1.45	1.23	**0.85**
	T600-L2-2	150	1.0	45.1	600	0.242	108	0.022	0.012	1.07	1.04	**0.97**	1.27	1.23	**0.97**
	T600-L2-3	150	1.0	45.1	600	0.242	108	0.022	0.012	1.05	1.04	**0.99**	1.24	1.23	**0.99**
	T400-L2-1	150	1.0	45.1	400	0.242	108	0.022	0.012	2.33	1.95	**0.84**	2.76	2.31	**0.84**
	T400-L2-2	150	1.0	45.1	400	0.242	108	0.022	0.012	1.61	1.95	**1.22**	1.90	2.31	**1.22**
	T400-L2-3	150	1.0	45.1	400	0.242	108	0.022	0.012	2.54	1.95	**0.77**	3.00	2.31	**0.77**
	T200-L2-1	150	1.0	45.1	200	0.242	108	0.022	0.012	1.96	1.98	**1.01**	2.32	2.34	**1.01**
	T200-L2-2	150	1.0	45.1	200	0.242	108	0.022	0.012	2.62	1.98	**0.75**	3.10	2.34	**0.75**
	T200-L2-3	150	1.0	45.1	200	0.242	108	0.022	0.012	2.36	1.98	**0.84**	2.79	2.34	**0.84**
	T800-L3-1	150	1.0	45.1	800	0.363	108	0.022	0.021	0.87	0.83	**0.95**	0.80	0.75	**0.95**
	T800-L3-2	150	1.0	45.1	800	0.363	108	0.022	0.021	0.83	0.83	**1.00**	0.75	0.75	**1.00**
	T800-L3-3	150	1.0	45.1	800	0.363	108	0.022	0.021	0.96	0.83	**0.86**	0.87	0.75	**0.86**
	T600-L3-1	150	1.0	45.1	600	0.363	108	0.022	0.021	1.18	1.04	**0.88**	1.07	0.95	**0.88**
	T600-L3-2	150	1.0	45.1	600	0.363	108	0.022	0.021	1.14	1.04	**0.92**	1.03	0.95	**0.92**
	T600-L3-3	150	1.0	45.1	600	0.363	108	0.022	0.021	1.09	1.04	**0.96**	0.99	0.95	**0.96**
	T400-L3-1	150	1.0	45.1	400	0.363	108	0.022	0.021	1.76	1.95	**1.11**	1.60	1.78	**1.11**
	T400-L3-2	150	1.0	45.1	400	0.363	108	0.022	0.021	2.37	1.95	**0.83**	2.15	1.78	**0.83**
	T400-L3-3	150	1.0	45.1	400	0.363	108	0.022	0.021	2.07	1.95	**0.95**	1.88	1.78	**0.95**
	T200-L3-1	150	1.0	45.1	200	0.363	108	0.022	0.021	2.02	1.98	**0.98**	1.83	1.80	**0.98**
	T200-L3-2	150	1.0	45.1	200	0.363	108	0.022	0.021	2.49	1.98	**0.79**	2.26	1.80	**0.79**
	T200-L3-3	150	1.0	45.1	200	0.363	108	0.022	0.021	1.62	1.98	**1.22**	1.47	1.80	**1.22**
	T800-L4-1	150	1.0	45.1	800	0.484	108	0.022	0.030	1.02	0.83	**0.81**	0.77	0.62	**0.81**
	T800-L4-2	150	1.0	45.1	800	0.484	108	0.022	0.030	0.78	0.83	**1.07**	0.59	0.62	**1.07**
	T800-L4-3	150	1.0	45.1	800	0.484	108	0.022	0.030	0.83	0.83	**0.99**	0.63	0.62	**0.99**
	T600-L4-1	150	1.0	45.1	600	0.484	108	0.022	0.030	1.36	1.04	**0.76**	1.03	0.79	**0.76**
	T600-L4-2	150	1.0	45.1	600	0.484	108	0.022	0.030	1.11	1.04	**0.94**	0.84	0.79	**0.94**
	T600-L4-3	150	1.0	45.1	600	0.484	108	0.022	0.030	0.95	1.04	**1.09**	0.72	0.79	**1.09**
	T400-L4-1	150	1.0	45.1	400	0.484	108	0.022	0.030	1.80	1.95	**1.09**	1.36	1.47	**1.09**
	T400-L4-2	150	1.0	45.1	400	0.484	108	0.022	0.030	1.74	1.95	**1.12**	1.31	1.47	**1.12**
	T400-L4-3	150	1.0	45.1	400	0.484	108	0.022	0.030	1.69	1.95	**1.16**	1.27	1.47	**1.16**
	T200-L4-1	150	1.0	45.1	200	0.484	108	0.022	0.030	1.74	1.98	**1.13**	1.31	1.49	**1.13**
	T200-L4-2	150	1.0	45.1	200	0.484	108	0.022	0.030	2.01	1.98	**0.98**	1.52	1.49	**0.98**
	T200-L4-3	150	1.0	45.1	200	0.484	108	0.022	0.030	2.16	1.98	**0.92**	1.63	1.49	**0.92**
Bisby *et al.* [4]	**W686A**	150	1.0	28.0	686	0.120	241	0.017	0.022	0.82	0.77	**0.94**	0.70	0.66	**0.94**
	W686B	150	1.0	28.0	686	0.120	241	0.017	0.022	0.83	0.77	**0.93**	0.71	0.66	**0.93**
	W686C	150	1.0	28.0	686	0.120	241	0.017	0.022	0.60	0.77	**1.28**	0.51	0.66	**1.28**
	W686A	150	1.0	28.0	686	0.120	241	0.017	0.022	0.56	0.77	**1.38**	0.47	0.66	**1.38**
	W686B	150	1.0	28.0	686	0.120	241	0.017	0.022	0.68	0.77	**1.14**	0.58	0.66	**1.14**
	W686C	150	1.0	28.0	686	0.120	241	0.017	0.022	0.80	0.77	**0.97**	0.68	0.66	**0.97**
Song *et al.* [13]	**H800L2-1**	112	0.4	40.2	800	0.242	105	0.022	0.005	0.77	0.83	**1.08**	0.86	0.93	**1.08**
	H800L2-2	112	0.4	40.2	800	0.242	105	0.022	0.005	0.81	0.83	**1.02**	0.91	0.93	**1.02**
	H800L2-3	112	0.4	40.2	800	0.242	105	0.022	0.005	0.84	0.83	**0.99**	0.94	0.93	**0.99**
	H600L2-1	112	0.4	40.2	600	0.242	105	0.022	0.005	1.04	1.04	**1.00**	1.17	1.16	**1.00**
	H600L2-2	112	0.4	40.2	600	0.242	105	0.022	0.005	1.05	1.04	**0.99**	1.17	1.16	**0.99**
	H600L2-3	112	0.4	40.2	600	0.242	105	0.022	0.005	0.95	1.04	**1.09**	1.07	1.16	**1.09**
	H400L2-1	112	0.4	40.2	400	0.242	105	0.022	0.005	2.03	1.95	**0.96**	2.27	2.19	**0.96**
	H400L2-2	112	0.4	40.2	400	0.242	105	0.022	0.005	1.99	1.95	**0.98**	2.22	2.19	**0.98**
	H400L2-3	112	0.4	40.2	400	0.242	105	0.022	0.005	1.94	1.95	**1.01**	2.17	2.19	**1.01**
	H200L2-1	112	0.4	40.2	200	0.242	105	0.022	0.005	2.21	1.98	**0.90**	2.47	2.21	**0.90**
	H200L2-2	112	0.4	40.2	200	0.242	105	0.022	0.005	2.28	1.98	**0.87**	2.55	2.21	**0.87**
	H200L2-3	112	0.4	40.2	200	0.242	105	0.022	0.005	2.32	1.98	**0.85**	2.59	2.21	**0.85**
	H800L3-1	112	0.4	40.2	800	0.363	105	0.022	0.008	0.69	0.83	**1.21**	0.59	0.71	**1.21**
	H800L3-2	112	0.4	40.2	800	0.363	105	0.022	0.008	0.88	0.83	**0.94**	0.76	0.71	**0.94**
	H800L3-3	112	0.4	40.2	800	0.363	105	0.022	0.008	0.91	0.83	**0.91**	0.78	0.71	**0.91**
	H600L3-1	112	0.4	40.2	600	0.363	105	0.022	0.008	1.08	1.04	**0.97**	0.93	0.89	**0.97**
	H600L3-2	112	0.4	40.2	600	0.363	105	0.022	0.008	1.31	1.04	**0.80**	1.12	0.89	**0.80**
	H600L3-3	112	0.4	40.2	600	0.363	105	0.022	0.008	1.06	1.04	**0.98**	0.91	0.89	**0.98**
	H400L3-1	112	0.4	40.2	400	0.363	105	0.022	0.008	1.67	1.95	**1.17**	1.43	1.68	**1.17**
	H400L3-2	112	0.4	40.2	400	0.363	105	0.022	0.008	1.55	1.95	**1.26**	1.33	1.68	**1.26**
	H400L3-3	112	0.4	40.2	400	0.363	105	0.022	0.008	1.51	1.95	**1.30**	1.29	1.68	**1.30**
	H200L3-1	112	0.4	40.2	200	0.363	105	0.022	0.008	1.70	1.98	**1.16**	1.46	1.70	**1.16**
	H200L3-2	112	0.4	40.2	200	0.363	105	0.022	0.008	1.91	1.98	**1.04**	1.64	1.70	**1.04**
	H200L3-3	112	0.4	40.2	200	0.363	105	0.022	0.008	2.00	1.98	**0.99**	1.71	1.70	**0.99**
	H800L4-1	112	0.4	40.2	800	0.484	105	0.022	0.012	0.75	0.83	**1.10**	0.53	0.59	**1.10**
	H800L4-2	112	0.4	40.2	800	0.484	105	0.022	0.012	0.89	0.83	**0.93**	0.64	0.59	**0.93**
	H800L4-3	112	0.4	40.2	800	0.484	105	0.022	0.012	0.89	0.83	**0.93**	0.64	0.59	**0.93**
	H600L4-1	112	0.4	40.2	600	0.484	105	0.022	0.012	1.31	1.04	**0.80**	0.93	0.74	**0.80**
	H600L4-2	112	0.4	40.2	600	0.484	105	0.022	0.012	1.18	1.04	**0.88**	0.84	0.74	**0.88**

(*continued on next page*)

Table 7 (*continued*)

Reference ID	Influential parameters								Experimental and analytical results					
	b (mm)	R_b	f_{c0} (MPa)	T_m (°C)	$n_f \times t_f$ (mm)	E_f (GPa)	ε_{fu}	$\rho_{k,f}$	$\eta_T{}^{Exp}$	$\eta_T{}^{Ana}$	$\frac{\eta_T{}^{Ana}}{\eta_T{}^{Exp}}$	$\nu_{s,max}^{T\ Exp}$	$\nu_{s,max}^{T\ Ana}$	$\frac{\nu_{s,max}^{T\ Ana}}{\nu_{s,max}^{T\ Exp}}$
H600L4-3	112	0.4	40.2	600	0.484	105	0.022	0.012	1.17	1.04	**0.89**	0.83	0.74	**0.89**
H400L4-1	112	0.4	40.2	400	0.484	105	0.022	0.012	1.78	1.95	**1.10**	1.27	1.39	**1.10**
H400L4-2	112	0.4	40.2	400	0.484	105	0.022	0.012	1.68	1.95	**1.17**	1.19	1.39	**1.17**
H400L4-3	112	0.4	40.2	400	0.484	105	0.022	0.012	1.39	1.95	**1.40**	0.99	1.39	**1.40**
H200L4-1	112	0.4	40.2	200	0.484	105	0.022	0.012	2.19	1.98	**0.90**	1.56	1.41	**0.90**
H200L4-2	112	0.4	40.2	200	0.484	105	0.022	0.012	1.67	1.98	**1.18**	1.19	1.41	**1.18**
H200L4-3	112	0.4	40.2	200	0.484	105	0.022	0.012	1.67	1.98	**1.18**	1.19	1.41	**1.18**

Nonetheless, above this axial strain level, as a consequence of the degeneration of micro-into meso- and macro-cracks along with heat-induced damage in the concrete, the volumetric change evolution was suddenly reversed triggering an abrupt increase in volumetric expansion. Fig. 4c also shows that for T600-L2 and T800-L2, compared to the other cases, larger axial strains were obtained for a certain Poisson's ratio. Furthermore, a closer evaluation of the data demonstrates that the maximum secant Poisson's ratio decreases significantly with increasing thermal damage, which can be attributed to the substantial contribution of the heat-induced damage level in the establishment of dilation behavior of HC. Accordingly, by applying a certain level of axial loading, the heat-induced damage leads to an additional axial strain in HC columns, and alters their transverse expansibility, dependent strongly on thermal damage level. The comparison of dilation responses shown in Fig. 4a and d confirms a significant reduction in terms of lateral strain by increasing FRP thickness (confinement stiffness), predominantly beyond the transition zone. Fig. 4e reveals that an increase in confinement stiffness leads to shorter volumetric expansion due to the stronger restrictions imposed to the concrete expansibility. The relations of ν_s and ε_c shown in Fig. 4f also confirms this behavior, where the specimens with more FRP thickness experienced a lower value of ν_s than those with less thickness (Fig. 4c).

In this study, it is aimed to extend the dilation model of Shayanfar et al. [8,17] originally suggested for FRP confined AC specimens to the case of FRP confined HC column through formulating the relation between ν_s^T and ε_c at different levels of heat-induced damage (T_m) based on regression analysis. For this purpose, a dataset of the dilation responses obtained from existing experimental data was collected as presented by Table 7. It should be noted that the following criteria were adopted to include/exclude experimental data: 1) ones obtained from concentric loading tests were included; 2) Specimens with a full confinement of unidirectional fibers installed transversely to the axial compression direction were included; 3) Specimens with helical wrapping configuration or hybrid confinement arrangements were excluded; 4) specimens of rectangular cross-section with transverse and longitudinal steel reinforcements were excluded; 5) ones registered experimentally with incomplete documented information, i.e. maximum exposure temperature, geometry details and material properties, were excluded; 6) ones obtained from test specimens with a premature failure mode caused by FRP debonding were excluded. In this table, $\nu_{s,\max}^T$ represents the peak Poisson's ratio of HC columns confined by FRP. η_T defines the ratio of $\nu_{s,\max}^T$ to $\nu_{s,\max}^A$ (where $\nu_{s,\max}^A$ is the peak Poisson's ratio of FRP confined AC columns at ambient temperature). For the calculation of $\nu_{s,\max}^A$, in the present study, the confinement stiffness-based model developed by Shayanfar et al. [17] was followed, which is determined as a main function of the confinement stiffness ($\rho_{K,f}$), namely:

$$\nu_{s,\max}^A = \frac{0.25}{\left(1 + L_{d0}/D_{eq}\right)\sqrt{\rho_{K,f}}} \tag{23}$$

in which (by considering Eqs. (10), (15) and (16))

$$\rho_{K,f} = K_V I_f = K_e \frac{n_f t_f E_f}{550 D_{eq} f_{c0}{}^{0.75}} \tag{24}$$

$$0.57 \le \frac{L_{d0}}{\sqrt{A_g}\psi_f} = 1.71 - 3.53 \times 10^{-5} A_g \le 1.36 \tag{25}$$

$$\psi_f = \frac{6.3}{\sqrt{f_{c0}}} \le 1 \tag{26}$$

where L_{d0} is the compression damage zone length of unconfined concrete columns which was determined as recommended by Lertsrisakulrat et al. [50]; A_g is the total area of the column's cross section.

For the determination of $\nu_{s,\max}^T$, it can be considered a function of $\nu_{s,\max}^A$ by

$$\nu_{s,\max}^T = \frac{\nu_{s,\max}^T}{\nu_{s,\max}^A}\nu_{s,\max}^A = \eta_T \nu_{s,\max}^A \tag{27}$$

Therefore, by calculating $\nu_{s,\max}^A$ using Eq. (23) for the specimens

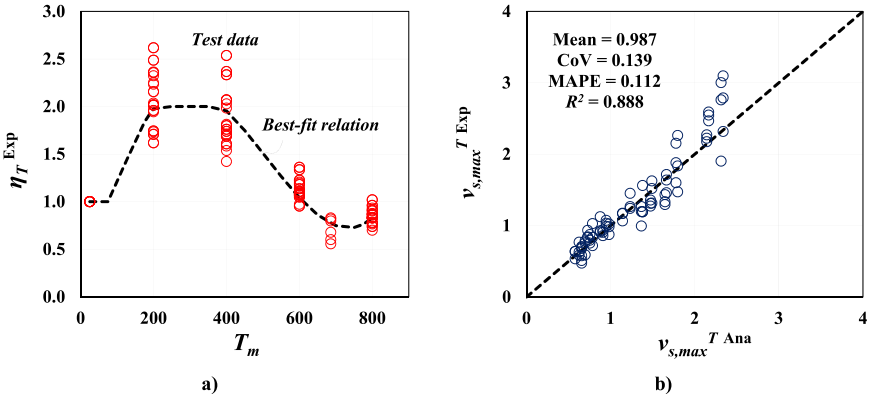

Fig. 5. a) Variation of η_T with respect to T_m; b) Predictive performance of Eqs. (27) and (28).

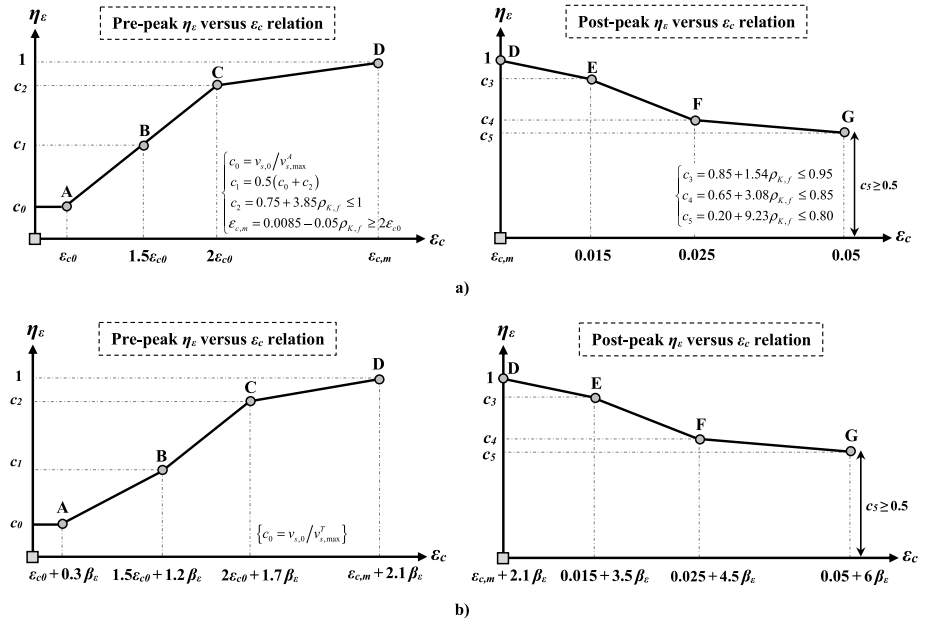

Fig. 6. Relation between η_ε versus ε_c; a) at ambient conditions; b) at elevated temperature
Note: In Fig. 6b, c_1, c_2, c_3, c_4 and c_5 are the same as presented in Fig. 6a.

assembled in the database, their corresponding values of η_T can be obtained as $\eta_T^{Exp} = v_{s,\max}^{T\ Exp}/v_{s,\max}^{A}$ (Table 7). Fig. 5a shows the variation of η_T^{Exp} with respect to T_m. As can be seen, by increasing T_m in the interval $25-400°C$, η_T^{Exp} significantly increases up to the peak, while for $T_m > 400°C$, a noticeable reduction of η_T^{Exp} with the increase of T_m is observed. Based on the best-fit relation obtained from regression analysis performed on 78 experimental data, the following equation was derived for determining η_T from T_m and R_b (Fig. 5a):

$$\eta_T = \frac{33.2\left(\frac{T_m}{1000}\right)^3 - 51\left(\frac{T_m}{1000}\right)^2 + 21.2\left(\frac{T_m}{1000}\right) - 0.49}{1.65 - 0.65R_b} \geq 1 \quad \text{for } T_m \leq 100°C \tag{28a}$$

$$\eta_T = \frac{33.2\left(\frac{T_m}{1000}\right)^3 - 51\left(\frac{T_m}{1000}\right)^2 + 21.2\left(\frac{T_m}{1000}\right) - 0.49}{1.65 - 0.65R_b} \leq 2 \quad \text{for } 100°C < T_m \leq 800°C \tag{28b}$$

where the developed expression is valid for $T_m \leq 800°C$ based on the interval of the submitted maximum exposure temperatures ($T_m = [25°C,$

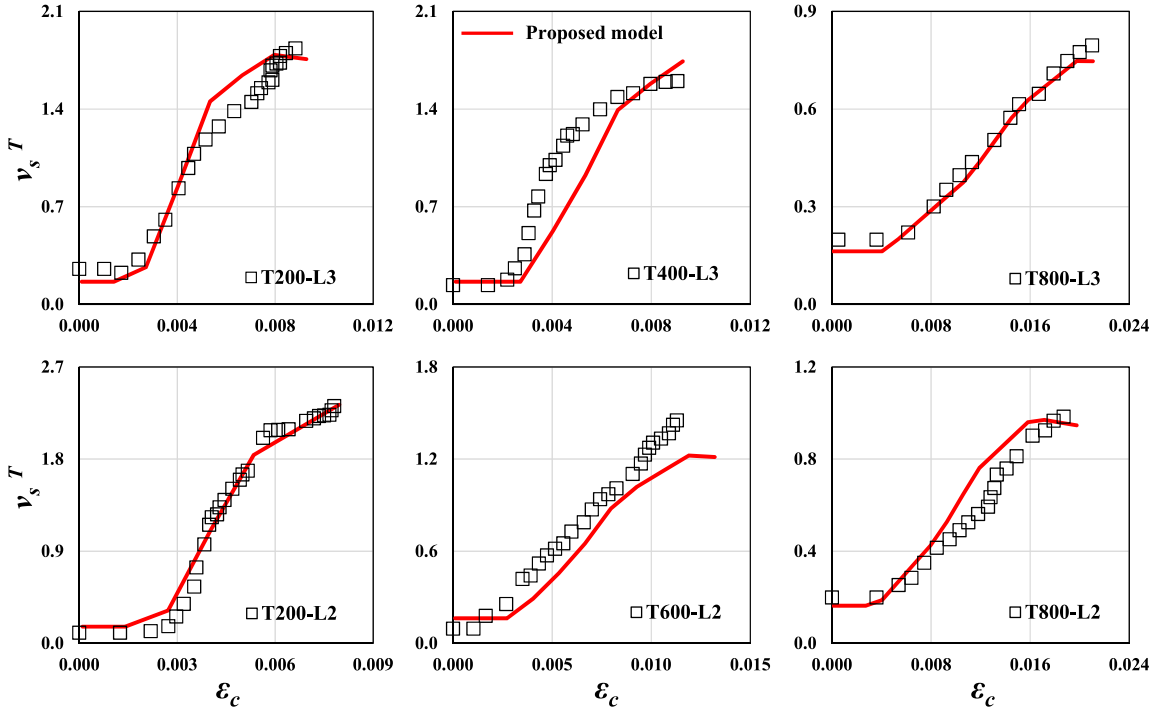

Fig. 7. Comparisons of the model predictions with the test results (Ouyang et al. [12]).

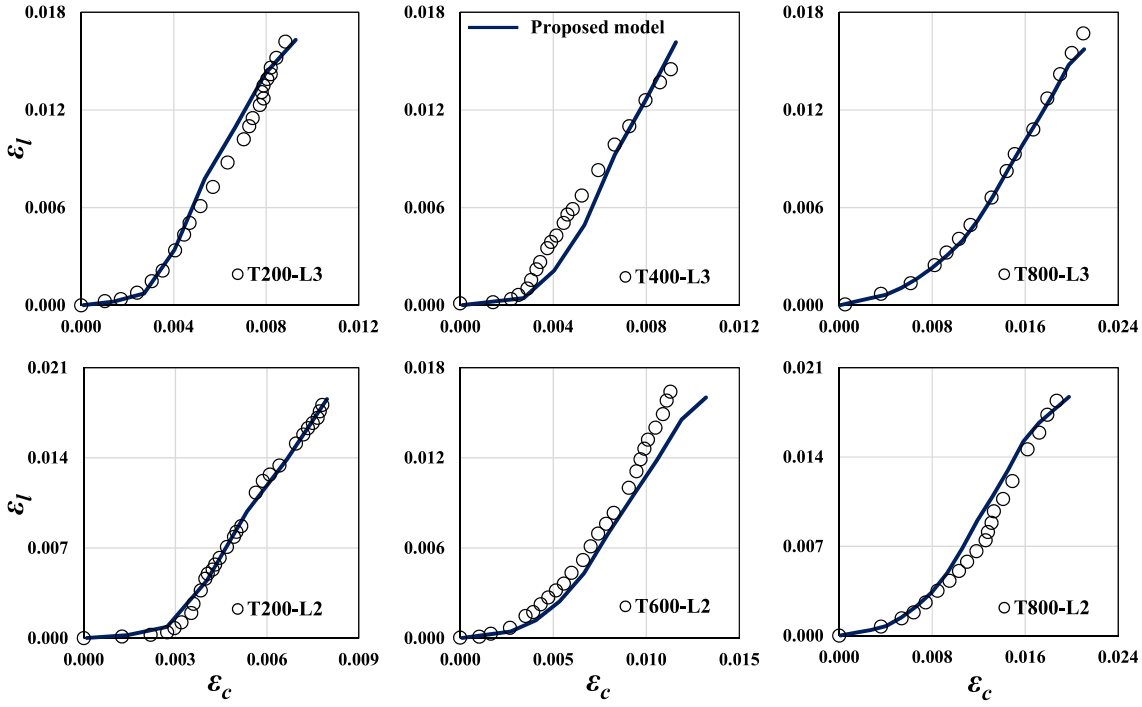

Fig. 8. Comparisons of the model predictions with the test results (Ouyang et al. [12]).

800 °C]) in the database used for the regression analysis. Therefore, by addressing $\nu^A_{s,\max}$ and η_T in Eq. (27) through Eqs. 23 and 28, the peak Poisson's ratio of FRP confined HC columns ($\nu^T_{s,\max}$) can be calculated. Fig. 5b evaluates the performance of Eq. (27). Based on the obtained assessment indicators, the established expression revealed a good predictive performance.

For the determination of Poisson's ratio of HC columns confined by FRP (ν^T_s) during axial loading, ν^T_s is considered as a function of $\nu^T_{s,\max}$, resulting in

$$\nu^T_s = \frac{\nu^T_s}{\nu^T_{s,\max}}\nu^T_{s,\max} = \eta_\varepsilon \nu^T_{s,\max} \tag{29}$$

where η_ε represents the ratio of ν^T_s and $\nu^T_{s,\max}$ at a given axial strain (ε_c). Introducing Eq. (27) into Eq. (29), ν^T_s is suggested by

$$\nu^T_s = \eta_\varepsilon \eta_T \nu^A_{s,\max} \tag{30}$$

To calculate ν^T_s by Eq. (30), η_ε needs to be addressed as an input parameter. For the determination of η_ε at a given level of ε_c for FRP confined AC columns (at ambient condition), Shayanfar et al. [8] proposed a simple but reliable multilinear model as shown in Fig. 6a in this figure, c_0 c_1, c_2, c_3, c_4 and c_5 are the calibration factors reflecting the influence of confinement stiffness on η_ε versus ε_c relation; $\varepsilon_{c,m}$ represents the axial strain corresponding to $\nu^A_{s,\max}$; $\nu_{s,0}$ is the initial Poisson's coefficient of unconfined AC columns, which was determined by (Candappa et al. [51]):

$$\nu_{s,0} = 8\times10^{-6}{f_{c0}}^2 + 2\times10^{-4}f_{c0} + 0.138 \tag{31}$$

As can be seen in Fig. 6a, the pre- and post-peak phases are dependent of ρ_{Kf}. The pre-peak relation demonstrates that concrete initially behaves similar to unconfined AC column with initial Poisson's coefficient as $\nu_{s,0}$. Afterward ($\varepsilon_c > \varepsilon_{c0}$), η_ε increases up to the peak stage ($\eta_\varepsilon = 1$) at $\varepsilon_{c,m}$. The post-peak relation shows that η_ε decreases with the increase of ε_c, whose reduction magnitude is dependent on ρ_{Kf}. In the present study, the relation developed by Shayanfar et al. [8] was extended for the case of FRP confined HC columns. For this purpose, as presented in Fig. 6b, a new relation of η_ε versus ε_c was developed where the influence of thermal damage was reflected by the parameter β_ε.

$$\beta_\varepsilon = \beta_\rho\left(\varepsilon^T_{c0} - \varepsilon_{c0}\right) \tag{32}$$

in which

$$0.4 \le \beta_\rho = 11{\rho_{Kf}}^{0.75} \le 1.4 \tag{33}$$

Accordingly, by calculating β_ε through Eq. (32), η_ε at a given ε_c can be obtained from the data presented in Fig. 6b. Then, the corresponding ν^T_s can be calculated by Eq. (30). To evaluate the reliability of the proposed relation, the results obtained from the experiments conducted by Ouyang et al. [12] and those determined by Eq. (30) are compared Fig. 7. As can be seen, the model has a good agreement with the experimental counterparts.

To obtain ε^T_l versus ε_c response of FFCC-H/FFSC-H based on the developed dilation model, the calculation procedure is summarized as:

1. Determine K_e using Eqs. (10), (11) and (16)
2. Determine ρ_{Kf} using Eq. (24)
3. Determine $\nu^A_{s,\max}$ using Eq. (23)
4. Determine η_T using Eq. (28)
5. Assume a value for axial strain (ε_c)
6. Determine β_ε using Eqs. (32), (5) to (7)
7. Determine η_ε using the developed multilinear model in Fig. 6b
8. Determine ν^T_s using Eq. (29)
9. Determine ε^T_l as $\varepsilon^T_l = \nu^T_s\varepsilon_c$
10. Continue the steps 5 to 9 up to the aim maximum value of ε_c, resulting a ε^T_l versus ε_c relation.

For the assessment of the model capability in the prediction of dilation response, Fig. 8 compares ε^T_l versus ε_c relations extracted from the experimental tests conducted by Ouyang et al. [12] and those simulated by the proposed model. As shown, the experimental results were simulated suitably by the model confirming its reliable predictive performance.

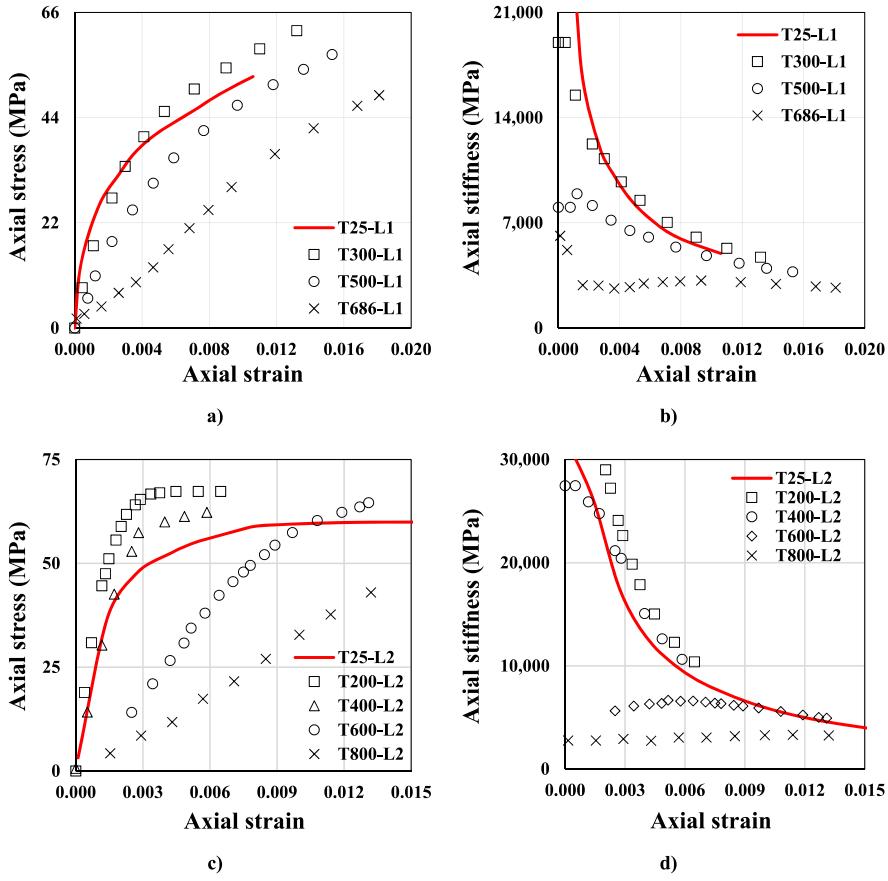

Fig. 9. Influence of the maximum temperature exposure on the a) and c) axial compressive stress-strain response; b) and d) secant stiffness versus axial compressive strain.
Note: The results indicted by Fig. 9a and b, and Fig. 9c and d were obtained from Bisby et al. [4] and Ouyang et al. [12], respectively. The results related to T25-L2 in Fig. 9c and d were determined based on the model developed by Shayanfar et al. [17].

4. Axial compressive stress-strain relation

Fig. 9 demonstrates the remarkable influence of the exposure temperature on the axial response of HC columns fully confined by FRP, tested by Bisby et al. [4] and Ouyang et al. [12]. As can be seen in Fig. 9a for the case of the results reported by Bisby et al. [4], compared to T25-L1 (control experimental specimen), even though T300-L1 experienced a slight heat-induced reduction in terms of initial axial stiffness, it showed higher axial strength and deformability. For T500-L1, heat-induced damage did not lead to a significant difference in the axial stress versus axial strain relationship. However, for the case of severely heat-damaged specimens (T686-L1), there is a noticeable reduction in its axial stiffness, compared to T25-L1. Moreover, the axial stress versus axial strain relationship of T686-L1 was almost linear, compared to almost bi-linear curves of specimens with the exposure temperatures lower than or equal to 500 °C. From the secant axial stiffness versus axial strain curves in Fig. 9b, T25-L1, T300-L1 and T500-L1 presented a reduction of the axial stiffness during the axial compressive loading. However, in T686-L1, after an initial relatively small reduction of the stiffness, it was preserved almost constant during the loading process, a consequence of the confinement effect provided by the FRP. The assessment of the exposure temperature effects on the test specimens conducted by Ouyang et al. [12] revealed that the axial strength and stiffness of specimens subjected up to 400 °C were higher than of T25-L2. It can be attributed to earlier activation of confining system in the cases of HC than AC due to the increase of concrete expansibility caused by the heat-induced damage. However, by increasing the temperature above that limit of 400 °C, thermal-induced damage increases significantly the axial deformation of the concrete specimen, converting a bi-linear stress-strain response into a linear one (Fig. 9c), and consequently an almost constant axial stiffness during axial loading process (Fig. 9d). Accordingly, the experimental results presented in Fig. 9 evidence the imperious impact of exposure maximum temperatures on the axial stress-strain response of FRP confined HC columns.

In order to calculate the axial stress versus axial strain relationship (f_c^A *vs* ε_c curve) of FRP passively confined AC columns (passively-confined-concrete), *Active Confinement Approach* (i.e. [14–17,52–54] can be followed. In this approach, the axial response of concrete with passive confinement is derived based on that of actively-confined-concrete subjected to a constant confinement pressure during the entire axial loading history. Accordingly, f_c^A corresponding to ε_c at a certain level of FRP confinement pressure ($f_{l,f}^A$) can be calculated by adopting an axial stress-strain base relation model ($f_c^A = g_1(f_{cc}^A, \varepsilon_c)$) coupled with an axial strength model, also known as failure surface function, ($f_{cc}^A = g_2(f_{l,f}^A)$) developed for actively-confined-concrete. Here, f_{cc}^A is the peak axial strength of axial stress-strain base relation model (defined from function g_1). However, since actively-confined-concrete case is under a constant $f_{l,f}^A$ during the entire axial loading history, contrary to passively-confined-concrete, the studies [15–17] evidenced that the original *Active Confinement Approach* overestimates the FRP-induced enhancement of passively-confined-concrete, which is generally recognized as *Confinement Path Effect*. To consider this effect, by adopting functions g_1 and g_2 from those exclusively developed for actively-confined-concrete, Lim and Ozbakkaloglu [15] recommended a reduction factor in the confinement-induced enhancements obtained for actively-confined-concrete, by decreasing the level of the confinement pressure $f_{l,f}^A$ in the function g_2. Shayanfar et al. [16and17] proposed a new axial strength framework model (function g_2) exclusively suggested for passively-confined-concrete to predict enhancements offered by a passive confining system.

In the present paper, for the calculation of f_c^A and ε_c relation of FRP confined AC columns taking into account *confinement path effect*, the

model developed by Shayanfar et al. [17] presenting a unified character for both full and partial confinement configurations and both circular and square cross-sections, is followed. In this model, the axial stress-strain base framework ($f_c{}^A$ versus ε_c relation using function g_1) is given by:

$$f_c{}^A = f_{cc}{}^A \frac{(\varepsilon_c/\varepsilon_{cc}{}^A) n_A}{n_A - 1 + (\varepsilon_c/\varepsilon_{cc}{}^A)^{n_A}} \tag{34}$$

in which

$$\frac{f_{cc}{}^A}{f_{c0}} = 1 + \frac{R_1}{R_2}\left(\frac{f_{l,f}{}^A}{f_{c0}}\right)^{R_2} \tag{35}$$

$$\frac{\varepsilon_{cc}{}^A}{\varepsilon_{c0}} = 1 + 5\left(\frac{f_{cc}{}^A}{f_{c0}} - 1\right) \tag{36}$$

$$n_A = \frac{E_c}{E_c - \frac{f_{cc}{}^A}{\varepsilon_{cc}{}^A}} \simeq \frac{1}{1 - 2.1 \times 10^{-4}\psi_A} \geq 1.1 \tag{37}$$

$$\psi_A = \frac{f_{cc}{}^A}{\varepsilon_{cc}{}^A \sqrt{f_{c0}}} \tag{38}$$

where $f_{cc}{}^A$ and $\varepsilon_{cc}{}^A$ are the peak axial strength and its corresponding axial strain, calibrated based on experimental AC specimens with passively confining system; R_1 and R_2 are the calibration factors in the determination of $f_{cc}{}^A$; n_A is the concrete brittleness at the ambient condition depending on ψ_A, as recommended by Carreira and Chu [55]. Accordingly, at a certain level of ε_c, $f_{cc}{}^A$ can be determined as a function of $f_{l,f}{}^A$ based on Eq. (35), and $\varepsilon_{cc}{}^A$ can be, subsequently, calculated by Eq. (36), as input parameters for the determination of $f_c{}^A$ by Eq. (34).

In this study, the model developed by Shayanfar et al. [17] was extended to be applicable for the establishment of axial response of the concrete being subjected to a certain exposure temperature. Accordingly, by substituting the mechanical characteristics of HC column with those of AC column, at a certain level of ε_c leading to FRP confinement pressure ($f_{l,f}^T$), axial stress-strain base relation model ($f_c{}^T$ versus ε_c curve using function g_1) can be expressed as:

$$f_c^T = f_{cc}^T \frac{(\varepsilon_c/\varepsilon_{cc}^T) n_T}{n_T - 1 + (\varepsilon_c/\varepsilon_{cc}^T)^{n_T}} \tag{39}$$

in which

$$n_T = \frac{1}{1 - 2.1 \times 10^{-4}\psi_T} \geq 1.1 \quad \text{for } T_m \leq 400^\circ\text{C} \tag{40a}$$

$$n_T = 2 - \frac{1 - 4.2 \times 10^{-4}\psi_T}{1 - 2.1 \times 10^{-4}\psi_T}\left(2 - \frac{T_m}{400}\right) \geq 1.1 \quad \text{for } 400^\circ\text{C} \leq T_m \leq 800\ ^\circ\text{C} \tag{40b}$$

$$\psi_T = \frac{f_{cc}^T}{\varepsilon_{cc}^T \sqrt{f_{c0}^T}} \tag{41}$$

where f_{cc}^T and ε_{cc}^T are the peak axial strength and its corresponding axial strain at a certain level of ε_c as input parameters for the axial stress-strain base relation model. n_T is the concrete brittleness that considers the influence of the maximum exposure temperature on f_{cc}^T, ε_{cc}^T and f_{c0}^T through the parameter ψ_T. Note that the axial stiffness of FRP confined HC columns with severe thermal-induced damages ($T_m \simeq 600 - 800^\circ$C) seems to be almost constant with a linear axial behavior during axial loading as demonstrated in Fig. 9. Accordingly, in the present study, n_T corresponding to $T_m = 800^\circ$C was assumed equal to a constant value of $n_T = 2$ during the entire loading history, adjusted based on the best-fit relation of the proposed model with the experimental axial stress-strain responses reported by Bisby et al. [4], Lenwari et al. [10], Ouyang et al. [12] and Song et al. [13]. Consequently, in Eq. (40b) ($400^\circ\text{C} \leq T_m \leq 800\ ^\circ\text{C}$), n_T was considered on the interval of the n_T obtained from Eq. (40a) for $T_m = 400^\circ$C and $n_T = 2$ corresponding to $T_m = 800^\circ$C, with a linear relationship with T_m.

For the establishment of ε_{cc}^T at high temperatures, the preliminary comparative assessment of the proposed model with ε_{cc}^T obtained based on Eq. (36) demonstrated a very significant underestimation in its model predictive performance, particularly for the cases with severe thermal-induced damages. On the other hand, based on experimental studies it was evidenced that the axial behavior of FRP confined HC columns tends to be similar to actively-confined-concrete due to more expansive behavior of HC than AC (Fig. 4). Therefore, the ε_{cc}^T of HC columns with high exposure temperature is calculated according to the approach proposed by Lim and Ozbakkaloglu [41], exclusively developed for the case of actively-confined-concrete:

$$\varepsilon_{cc}^T = \varepsilon_{c0}^T\left[1 + 5\left(\frac{f_{l,f}^T}{f_{c0}^T} - 1\right)\right] \quad \text{for } T_m \geq 100^\circ\text{C} \tag{42a}$$

$$\varepsilon_{cc}^T = \varepsilon_{c0}^T + 0.045\left(\frac{f_{l,f}^T}{f_{c0}^T}\right)^{1.15} + \lambda_\varepsilon \quad \text{for } 100^\circ\text{C} \leq T_m \leq 200\ ^\circ\text{C} \tag{42b}$$

$$\varepsilon_{cc}^T = \varepsilon_{c0}^T + 0.045\left(\frac{f_{l,f}^T}{f_{c0}^T}\right)^{1.15} \quad \text{for } T_m \geq 200^\circ\text{C} \tag{42c}$$

in which

$$\lambda_\varepsilon = \left[0.045\left(\frac{f_{l,f}^T}{f_{c0}^T}\right)^{1.15} - 5\varepsilon_{c0T}\left(\frac{f_{l,f}^T}{f_{c0}^T} - 1\right)\right]\left(\frac{T_m}{100} - 2\right) \tag{43}$$

In this study, a new axial strength model was developed, applicable to FRP confined HC columns, having a unified character with Eq. (35) when the concrete is under ambient conditions:

$$\frac{f_{cc}^T}{f_{c0}^T} = 1 + \frac{R_1}{R_2}\left(\overline{m}\frac{f_{l,f}^T}{f_{c0}^T}\right)^{R_2} + \frac{R_3}{R_4}\left(\frac{f_{l,f}^T}{f_{c0}^T}\right)^{R_4} \tag{44}$$

where R_1, R_2, R_3 and R_4 are the calibration factors in the determination of f_{cc}^T obtained from the regression analyses on FRP passively confined HC columns; $\overline{m}$ is the calibration factor reflecting the influence of more expansive behavior of the concrete with a certain level of thermal damage, which activates earlier the confining system compared to the AC column at ambient temperature (based on the comparative assessment on the dilation behavior of FFCC-H/FFSC-H presented in Fig. 4). In Eq. (44), the second term $\left(\frac{R_1}{R_2}\left(\overline{m}\frac{f_{l,f}^T}{f_{c0}^T}\right)^{R_2}\right)$ represents the improvements obtained from the confinement of an AC column with axial strength equal to f_{c0}^T, considering the effect of earlier activation (through $\overline{m}$) compared to AC; The third term $\left(\frac{R_3}{R_4}\left(\frac{f_{l,f}^T}{f_{c0}^T}\right)^{R_4}\right)$ in Eq. (44) considers the increase of confinement-induced improvements due to thermal-induced damage. Based on experimental axial stress versus axial strain relations, Shayanfar et al. [17] proposed new expressions to determine the calibration factors of R_1 and R_2, which was rearranged by substituting f_{c0} by f_{c0}^T:

$$R_1 = \frac{23.9}{\beta_{0T}{}^{0.5}\lambda_{fc}\lambda_{Rb}}\rho_{K,f}{}^{0.67} \leq 4.25 \tag{45}$$

$$R_2 = \frac{1.85}{\beta_{0T}{}^{0.2}}\rho_{K,f}{}^{0.26} \geq 0.3 \tag{46}$$

in which

$$\lambda_{fc} = 0.75 + 0.008\beta_{0T}f_{c0} \tag{47}$$

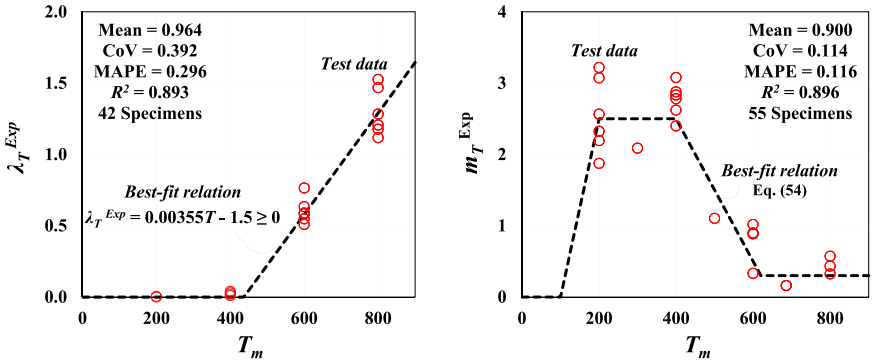

Fig. 10. a) Variation of λ_T^{Exp} with respect to T_m; b) Variation of m_T^{Exp} with respect to T_m.

$$\lambda_{Rb} = 1.5(1 - 1.1R_b) \geq 1 \tag{48}$$

where λ_{fc} and λ_{Rb} reflect the impact of concrete axial strength and the dimension of corner radius in the calibration of R_1, respectively. In order to determine the calibration factors of R_3 and R_4 representing the effect of thermal-induced damage in terms of confinement-induced enhancements, the experimental axial stress-strain responses reported by Bisby et al. [4], Lenwari et al. [10], Ouyang et al. [12] and Song et al. [13] were used for statistical modeling. Through regression analyses on the assembled data, the calibration factors R_3 and R_4 are determined from:

$$R_3 = \frac{\lambda_T}{\lambda_{rb}\lambda_K} \geq 0 \tag{49}$$

$$R_4 = 0.92\left(\frac{f_{l,f}^T}{f_{c0}^T}\right)^{0.1} \tag{50}$$

in which

$$\lambda_T = 3.55\left(\frac{T_m}{1000}\right) - 1.55 \geq 0 \tag{51}$$

$$\lambda_K = 1.15 - 0.022K_H\frac{n_f t_f E_f}{D_{eq} f_{c0}} \tag{52}$$

$$\lambda_{rb} = 1.22R_b^{0.25} \geq 0.85 \tag{53}$$

where λ_T, λ_K and λ_{rb} reflect the impact of maximum exposure temperature (T_m), confinement stiffness and the dimension of corner radius in the calibration of R_3, respectively. As shown in Fig. 10a, the developed model parameter (λ_T) provides a sufficient agreement with the experimental counterparts, which was determined based on the best-fit relation of the proposed model with the experimental axial stress-strain responses.

Due to the fact that pre-existing micro-cracks in thermally damaged concrete tend to activate passively confining system at the initial stage of axial compressive loading, the calibration factor of $\overline{m}$ was considered in the establishment of Eq. (44), having been obtained from regression analysis to enhance the confinement effectiveness, resulting:

$$\overline{m} = 1 + m_0 \exp\left(-11.2\frac{f_{l,f}^T}{f_{c0}^T}\right) \tag{54}$$

in which

$$m_0 = \frac{m_T}{m_\rho m_r} \tag{55}$$

$$0 \leq m_T = 0.025(T_m - 100) \leq 2.5 \quad \text{for } T_m \leq 400^\circ\text{C} \tag{56a}$$

$$m_T = 2.5 - 0.01(T_m - 400) \geq 0.3 \quad \text{for } T_m \geq 400^\circ\text{C} \tag{56b}$$

$$m_r = 0.3 + 0.7R_b \tag{57}$$

$$m_\rho = 0.2\beta_{0T}^{0.3}\rho_{K,f}^{-0.4} \tag{58}$$

where m_T, m_r and m_ρ are the calibration factors determined based on the regression analysis reflecting the effect of maximum exposure temperature (T_m), corner radius ratio (R_b) and confinement stiffness ($\rho_{K,f}$). As shown in Fig. 10b, the developed model parameter (m_T) has a good agreement with the experimental counterparts, which extracted based on Eqs. (51) and (52) ($m_T^{Exp} = m_\rho m_r \frac{\overline{m}^{Exp}-1}{\exp(-11.2 f_{l,f}^T/f_{c0}^T)}$ where $\overline{m}^{Exp}$ was determined using back analysis from the best fit of the experimental results of the axial stress-strain curve of test specimens with those obtained from the developed model).

5. Calculation process

In the following, the calculation methodology of the proposed model, which can be implemented into a spreadsheet, for determining the axial response of FRP confined concrete submitted to a certain level of thermal damage is presented. The calculation procedure is as.

1. Determine the mechanical characteristics of unconfined heat-damaged concrete:
   - Peak axial strength (f_{c0}^T) by Eq. (1)
   - Axial strain corresponding to f_{c0}^T (ε_{c0}^T) by Eq. (6)
2. Assume a value for ε_c on the interval (0, ε_{cu}] where ε_{cu} is the ultimate axial strain when FRP rupture occurs.
3. Determine the dilation response corresponding to ε_c
   - Secant Poisson's ratio (v_s^T) by Eq. (29) and the data presented in Fig. 6
   - Confinement pressure ($f_{l,f}^T$) by Eq. (22)
4. Determine the axial response corresponding to ε_c
   - Calibration factors R_1, R_2, R_3 and R_4, by Eqs. (45), (46), (49), and (50)
   - $\overline{m}$ factor from Eq. (54)
   - Peak axial strength (f_{cc}^T) by Eq. (44)
   - Axial strain (ε_{cc}^T) corresponding to f_{cc}^T by Eq. (42)
   - Axial stress (f_c^T) by Eq. (39)
5. Continue the aforementioned incremental procedure up to ε_{cu}, f_c^T versus ε_c relation can be calculated

Since the focus of the current study was given on the simulation of global axial stress-strain curves, the experimental values of ultimate axial strain (ε_{cu}) was used to terminate the computation process.

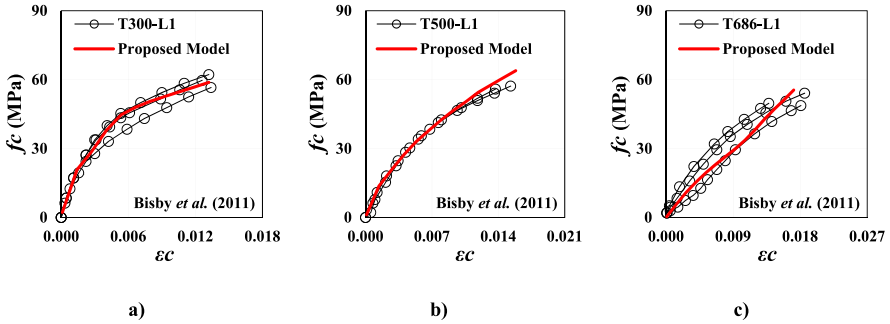

Fig. 11. Predictive performance of the proposed model using the test specimens conducted by Bisby et al. [4].
Note: Ti-Lj represents the test specimens submitted to exposure temperature *i*, and subsequently confined by *j* layer FRP jackets.

It is noteworthy that the reliability of regression analyses performed for developing predictive equations (as key components of the proposed model) is limited to the range of input/output variables supported in the used database. Accordingly, the predictive performance of these equations can be improved through recalibrating the model components based on new datasets consisting of the relevant variables with a broader range. Furthermore, the experimental data used for calibrating the failure surface function and the coupled dilation model was obtained from tests on relatively small FRP confined prototypes of square/circular concrete specimens where thermal distribution inside the concrete can be reasonably considered uniform. Therefore, for real cases with a larger dimension and non-uniform thermal distribution whose relative variables might not be in the aforementioned interval, the key components of the proposed model might need to be recalibrated, which will be the focus of a future study. Considering the relatively simple methodology of the proposed analytical-based model, it can be extended potentially to FRP confined heat-damaged RC columns of rectangular cross-section, through addressing properly the influences of dual FRP-steel confinement, sectional aspect ratio (the ratio of longer and shorter cross-section dimensions) and their interactions with exposure temperature in terms of axial and dilation behavior.

6. Verification

This section assesses the predictive performance of the developed analysis-oriented model for the prediction of axial response of concrete specimens submitted to a certain maximum exposure temperature, and after the specimens have attained the environmental temperature, subsequently, confined with FRP confining system. For this purpose, the axial stress-strain curve obtained from the proposed model is compared to that obtained from the experimental studies conducted by Bisby et al. [4], Lenwari et al. [10], Ouyang et al. [12] and Song et al. [13].

Bisby et al. [4] performed an experimental study to investigate the axial stress-strain response of FRP fully confined circular HC columns. The diameter and height of the test specimens were 100 mm and 200 mm, respectively. The axial compressive strength of AC column at the room temperature was 28 MPa. The values of nominal thickness, modulus of elasticity and rupture strain of CFRP jackets were reported as 0.12 mm, 241.1 GPa and 1.7%, respectively. All the specimens submitted to a certain level of maximum exposure temperature were confined by one CFRP layer. Complete details regarding the test specimens can be found from Bisby et al. [4]. Fig. 11 presents the comparison of the results obtained from the analytical model with those measured experimentally. As can be seen, the model has a good predictive performance in the estimation of axial responses of the test specimens submitted to 300 °C, 500 °C and 700 °C, even though there is a slight overestimation in terms of maximum axial strength for T500-L1.

Lenwari et al. [10] experimentally determined the axial stress-strain response of FRP fully confined circular HC columns. The diameter and height of the test specimens were 150 mm and 300 mm, respectively. The axial compressive strength of AC column at the room temperature was 40.5 MPa. The values of nominal thickness, modulus of elasticity and rupture strain of CFRP jackets were reported as 0.131 mm, 234.1 GPa and 1.8%, respectively. All the specimens submitted to a certain level of maximum exposure temperature were confined by one CFRP layer. Complete details regarding the test specimens can be found from Lenwari et al. [10]. Fig. 12 demonstrates the comparison of the results obtained from the analytical model with those measured experimentally. As can be seen, the model was able to predict the experimental counterparts with a good agreement, even though there is a slight overestimation in terms of maximum axial strength for T300-L1 and T500-L1.

For further investigation of the capability of the developed confinement model, the axial stress-strain curves obtained from experimental studies conducted by Ouyang et al. [12] and Song et al. [13], where the test specimens were submitted to a high level of thermal-induced damage ($T_m \geq 600°C$), are compared with those analytically obtained from the model, as shown in Figs. 13 and 14. As can be observed, the model could accurately predict the full range of the experimentally measured axial responses, except for a slight underestimation for the cases of T600-L3 and T600-L3 tested by Song et al. [13] (Fig. 14e and f).

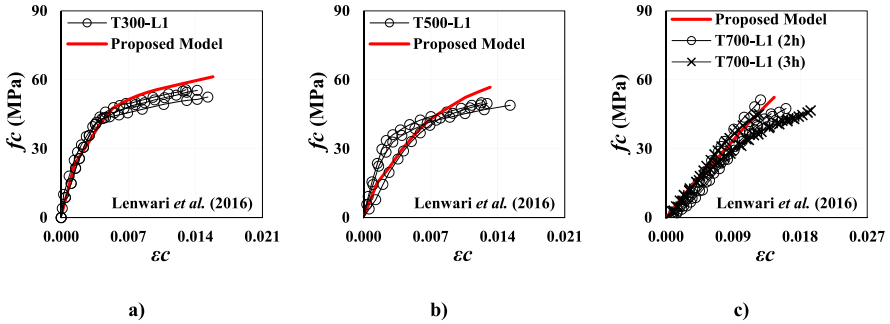

Fig. 12. Predictive performance of the proposed model using the test specimens conducted by Lenwari et al. [10].

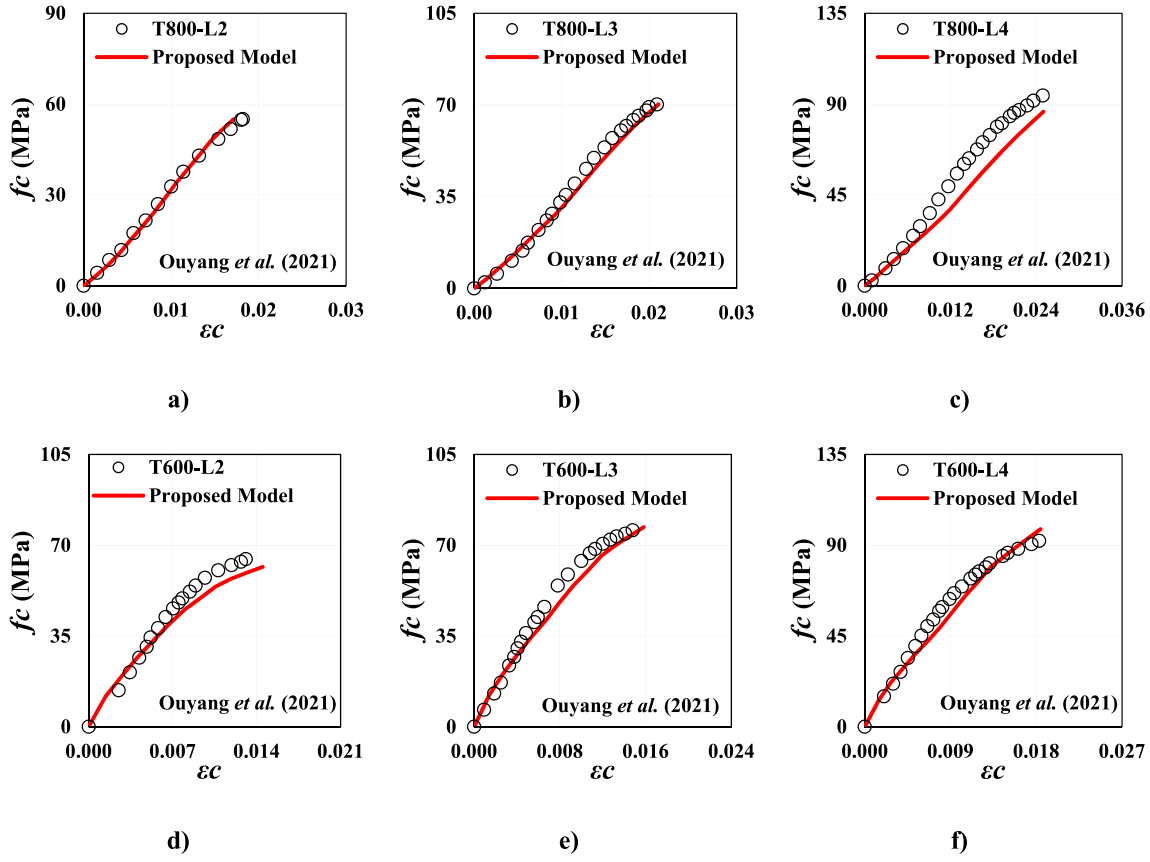

Fig. 13. Predictive performance of the proposed model using the test specimens conducted by Ouyang et al. [12].

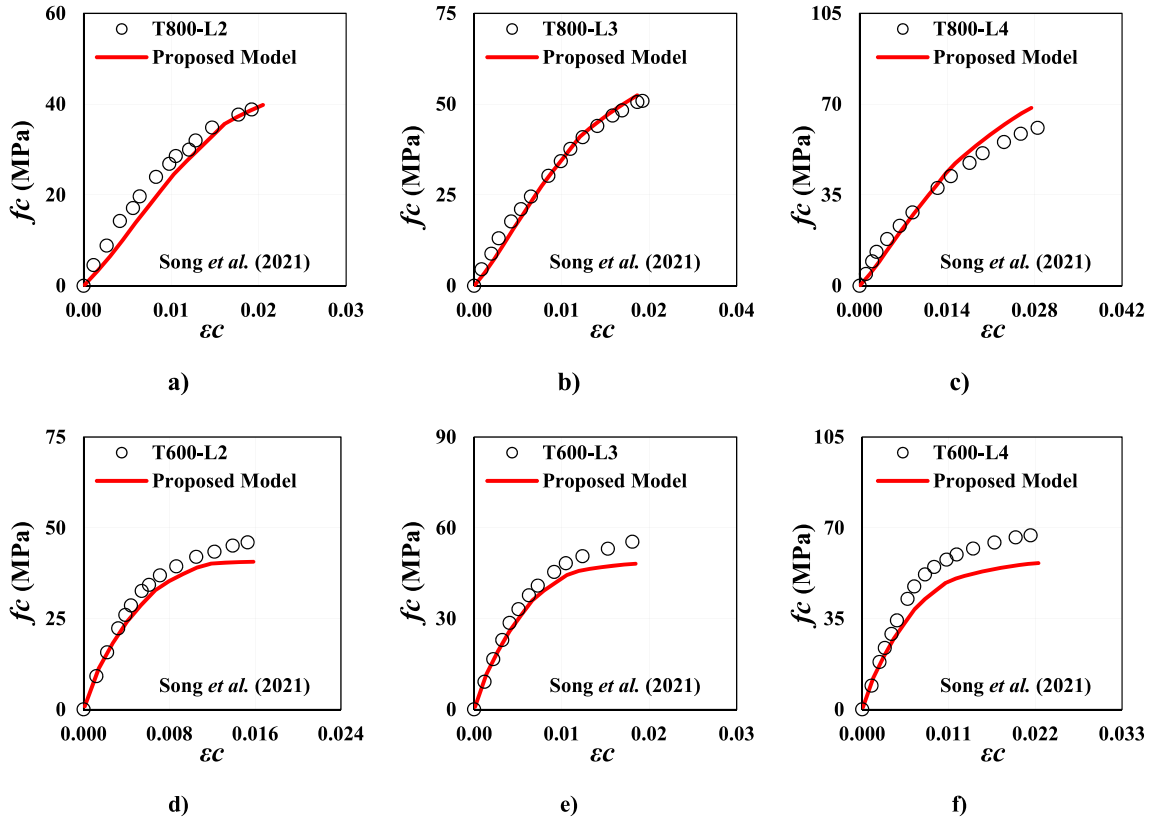

Fig. 14. Predictive performance of the proposed model using the test specimens conducted by Song et al. [13].

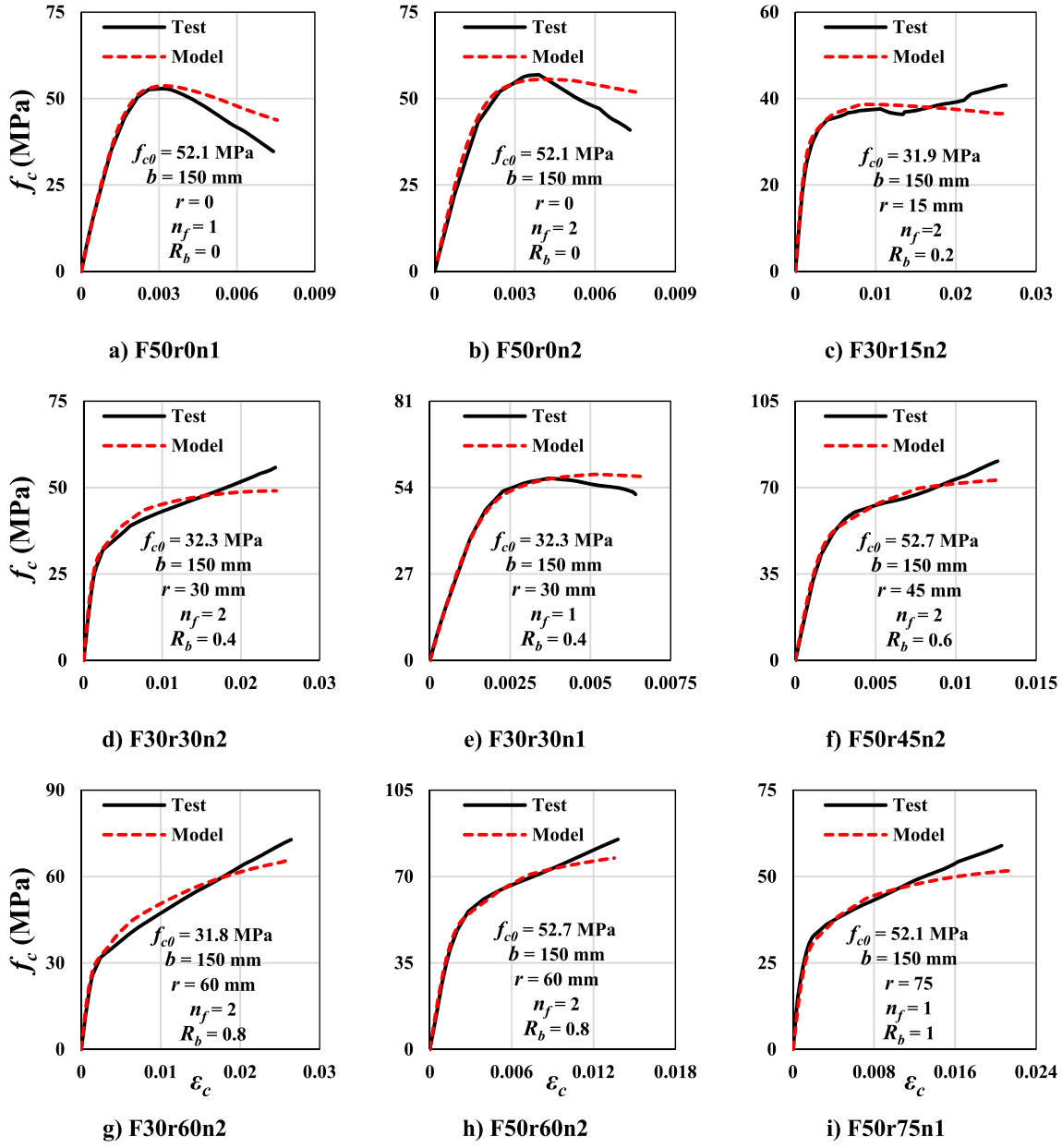

Fig. 15. Predictive performance of the proposed model using the test specimens conducted by Wang and Wu [6].

Due to the unified character of the proposed analysis-oriented model at ambient and elevated temperature conditions, Fig. 15 compares the axial stress-strain relations of FFSC-A reported from the experimental study conducted by Wang and Wu [6] with those analytically obtained from the model to assess its capability for the cases at ambient condition. All specimens had a section dimension of 150 mm and a height of 300 mm, with a sectional corner radius ratio (R_b) varying from 0 ($r = 0$) to 1 ($r = 75$ mm) representing a square cross section with sharp edges and circular cross-section, respectively. Two series of FFSC-A specimens with concrete strengths of $f_{c0} \simeq 30$ MPa and $f_{c0} \simeq 50$ MPa were tested. The CFRP thickness, tensile elastic modulus and rupture strain were 0.165 mm, 219 GPa, and 1.99%, obtained from flat coupon tensile tests. The complete details of the experimental program can be found in Wang and Wu [6]. As can be seen in Fig. 15, in general, there are a good agreement between the experimental axial stress-strain relationships with those obtained from the proposed model, confirming the successful simulation of the corner radius ratio (R_b) influence on confinement-induced enhancements of FFSC-A at ambient conditions.

7. Summary and conclusion

This paper has addressed the development of a new analysis-oriented model to predict the axial and dilation behavior of FRP confined HC circular/square concrete columns. Through regression analyses performed on a large database of unconfined heat-damaged concrete experimentally tested specimens, new expressions were developed to determine its mechanical characteristics in terms of axial compressive strength and its corresponding axial strain. A new model was developed to determine dilation response of FRP confined HC columns by formulating the effect of thermal damage level on Poisson's coefficient versus axial strain relationship. Subsequently, a new axial stress-strain model, coupled with the developed dilation model, was proposed to calculate the axial behavior of FRP confined HC columns with the different levels of maximum exposure temperature. Comparisons with axial and dilation results reported by available experiment studies in the literature verified that the developed analysis-oriented model is able to predict the experimental counterparts with good accuracy, and has a relatively

simple format for design purposes by using a data sheet.

CRediT author statement

Javad Shayanfar: Conceptualization, Methodology, Data curation, Validation, Writing- Original draft preparation; Joaquim A. O. Barros: Conceptualization, Methodology, Writing- Reviewing and Editing, Supervision; Mohammadali Rezazadeh: Conceptualization, Methodology, Writing- Reviewing and Editing, Supervision.

Declaration of competing interest

The authors declare that they have no known competing financial interests or personal relationships that could have appeared to influence the work reported in this paper.

Data availability

Data will be made available on request.

Acknowledgments

This study is a part of the project "*StreColesf_Innovative technique using effectively composite materials for the strengthening of rectangular cross-section reinforced concrete columns exposed to seismic loadings and fire*", with the reference POCI-01-0145-FEDER-029485. The first author also acknowledges the support provided by FCT PhD individual fellowship 2019 with the reference of "SFRH/BD/148002/2019".

References

[1] V. Kodur, Properties of concrete at elevated temperatures, ISRN Civ. Eng. (2014) 1–15.
[2] P. Bamonte, F. Lo Monte, Reinforced concrete columns exposed to standard fire: comparison among different constitutive models for concrete at high temperature, Fire Saf. J. 71 (2015) 310–323.
[3] U. Demir, M.F. Green, A. Ilki, Postfire seismic performance of reinforced precast concrete columns, PCI J. 65 (6) (2020).
[4] L.A. Bisby, J.F. Chen, S.Q. Li, T.J. Stratford, N. Cueva, K. Crossling, Strengthening fire-damaged concrete by confinement with fibre-reinforced polymer wraps, Eng. Struct. 33 (12) (2011) 3381–3391.
[5] J.A. Barros, D.R. Ferreira, Assessing the efficiency of CFRP discrete confinement systems for concrete cylinders, J. Compos. Construct. 12 (2) (2008) 134–148.
[6] L.M. Wang, Y.F. Wu, Effect of corner radius on the performance of CFRP-confined square concrete columns: test, Eng. Struct. 30 (2008) 493–505.
[7] W. Janwaen, J.A. Barros, I.G. Costa, A new strengthening technique for increasing the load carrying capacity of rectangular reinforced concrete columns subjected to axial compressive loading, Compos. B Eng. 158 (2019) 67–81.
[8] J. Shayanfar, M. Rezazadeh, J.A. Barros, Analytical model to predict dilation behavior of FRP confined circular concrete columns subjected to axial compressive loading, J. Compos. Construct. 24 (6) (2020), 04020071, 2020.
[9] B. Shan, F.C. Gui, G. Monti, Y. Xiao, Effectiveness of CFRP confinement and compressive strength of square concrete columns, J. Compos. Construct. 23 (6) (2019), 04019043, 2019.
[10] A. Lenwari, J. Rungamornrat, S. Woonprasert, Axial compression behavior of fire-damaged concrete cylinders confined with CFRP sheets, J. Compos. Construct. 20 (5) (2016), 04016027.
[11] X. Luo, W. Sun, S.Y.N. Chan, Effect of heating and cooling regimes on residual strength and microstructure of normal strength and high-performance concrete, Cement Concr. Res. 30 (3) (2000) 379–383.
[12] L.J. Ouyang, M.X. Chai, J. Song, L.L. Hu, W.Y. Gao, Repair of thermally damaged concrete cylinders with basalt fiber-reinforced polymer jackets, J. Build. Eng. 44 (2021), 102673.
[13] J. Song, W.Y. Gao, L.J. Ouyang, J.J. Zeng, J. Yang, W.D. Liu, Compressive behavior of heat-damaged square concrete prisms confined with basalt fiber-reinforced polymer jackets, Eng. Struct. 242 (2021), 112504.
[14] J. Teng, Y.L. Huang, L. Lam, L.P. Ye, Theoretical model for fiber-reinforced polymer-confined concrete, J. Compos. Construct. 11 (2) (2007) 201–210.
[15] J.C. Lim, T. Ozbakkaloglu, Unified stress-strain model for FRP and actively confined normal strength and high-strength concrete, J. Compos. Construct. 19 (4) (2014), 04014072, 2014.
[16] J. Shayanfar, J.A. Barros, M. Rezazadeh, Generalized Analysis-oriented model of FRP confined concrete circular columns, Compos. Struct. 270 (2021), 114026.
[17] J. Shayanfar, J.A. Barros, M. Rezazadeh, Unified model for fully and partially FRP confined circular and square concrete columns subjected to axial compression, Eng. Struct. 251 (2022), 113355.
[18] V.K.R. Kodur, M.A. Sultan, Effect of temperature on thermal properties of high-strength concrete, J. Mater. Civ. Eng. 15 (2) (2003) 101–107.
[19] K.D. Hertz, Concrete strength for fire safety design, Mag. Concr. Res. 57 (8) (2005) 445–453.
[20] N.K. Raut, V.K.R. Kodur, Response of high-strength concrete columns under design fire exposure, J. Struct. Eng. 137 (1) (2011) 69–79.
[21] F. Aslani, M. Bastami, Constitutive relationships for normal-and high-strength concrete at elevated temperatures, ACI Mater. J. 108 (4) (2011) 355.
[22] Y.F. Chang, Y.H. Chen, M.S. Sheu, G.C. Yao, Residual stress–strain relationship for concrete after exposure to high temperatures, Cement Concr. Res. 36 (2006) 1999–2005.
[23] Y.A. Al-Salloum, H.M. Elsanadedy, A.A. Abadel, Behavior of FRP-confined concrete after high temperature exposure, Construct. Build. Mater. 25 (2) (2011) 838–850.
[24] U. Sharma, K. Zaidi, N. Bhandari, Residual compressive stress-strain relationship for concrete subjected to elevated temperatures, J. Struct. Fire Eng. 3 (2012) 327–350.
[25] J. Geng, Q. Sun, W. Zhang, C. Lü, Effect of high temperature on mechanical and acoustic emission properties of calcareous-aggregate concrete, Appl. Therm. Eng. 106 (2016) 1200–1208.
[26] J. Xiao, Z. Li, Q. Xie, L. Shen, Effect of strain rate on compressive behaviour of high-strength concrete after exposure to elevated temperatures, Fire Saf. J. 83 (2016) 25–37.
[27] S. Xiang, L. Zeng, J. Zhang, J. Chen, Y. Liu, G. Cheng, J. Mo, A DIC-based study on compressive responses of concrete after exposure to elevated temperatures, Materials 12 (13) (2019) 2044.
[28] L.Y. Li, J. Purkiss, Stress–strain constitutive equations of concrete material at elevated temperatures, Fire Saf. J. 40 (7) (2005) 669–686.
[29] L.H. Han, J.S. Huo, Concrete-filled hollow structural steel columns after exposure to ISO-834 fire standard, J. Struct. Eng. 129 (1) (2003) 68–78.
[30] Eurocode 2: Design of Concrete Structures ENV EC2, 1992.
[31] T.T. Lie, T.D. Lin, Fire performance of reinforced concrete columns, in: ASTM STP 882. Fire Safety, Science and Engineering, 1985, pp. 176–205.
[32] T.T. Lie, T.J. Rowe, T.D. Lin, Residual Strength of Fire-Exposed Reinforced Concrete Columns, vol. 92, American Concrete Institute; Special Publication, Detroit, 1986, pp. 153–174.
[33] K.K.B. Dahl, Uniaxial Stress-Strain Curves for Normal and Highstrength concrete." ABK Rep. No. R282, Dept. of Structural Engineering, Technical Univ. of Denmark, Kongens Lyngby, Denmark. Eurocode 2: Design of Concrete Structures ENV EC2, 1992, 1992.
[34] D.C. Jansen, S.P. Shah, Effect of length on compressive strain softening of concrete, J. Eng. Mech. 123 (1) (1997) 25–35.
[35] K. Watanabe, J. Niwa, H. Yokota, M. Iwanami, Experimental study on stress-strain curve of concrete considering localized failure in compression, J. Adv. Concr. Technol. 2 (3) (2004) 395–407.
[36] Y. Wei, Y.F. Wu, Experimental study of concrete columns with localized failure, J. Compos. Construct. 20 (5) (2016), 04016032.
[37] Y.F. Wu, Y. Wei, Stress–strain modeling of concrete columns with localized failure: an analytical study, J. Compos. Construct. 20 (3) (2016), 04015071, 2016.
[38] K.H. Yang, Y. Lee, J.H. Mun, A stress-strain model for unconfined concrete in compression considering the size effect, Adv. Mater. Sci. Eng. 2019 (2019) 1–13.
[39] S. Popovics, A numerical approach to the complete stress-strain curve of concrete, Cement Concr. Res. 3 (5) (1973) 583–599.
[40] M.M. Karthik, J.B. Mander, Stress-block parameters for unconfined and confined concrete based on a unified stress-strain model, J. Struct. Eng. 137 (2) (2010) 270–273.
[41] J.C. Lim, T. Ozbakkaloglu, Stress–strain model for normal-and light-weight concretes under uniaxial and triaxial compression, Construct. Build. Mater. 71 (2014) 492–509, 2014.
[42] M.J. Terro, Numerical modeling of the behavior of concrete structures in fire, ACI Struct. J. 95 (No. 2) (1998) 183–193. Mar.-Apr.
[43] A. Khennane, G. Baker, Uniaxial model for concrete under variable temperature and stress, J Eng Mech-ASCE 119 (8) (1993) 1507–1525.
[44] P. Bazant, J.C. Chern, Stress-induced thermal and shrinkage strains in concrete, J Eng Mech-ASCE 113 (10) (1987) 1493–1511.
[45] T.T. Lie, Structural Fire Protection, American Society of Civil Engineers, New York, 1992.
[46] A. Mirmiran, M. Shahawy, Dilation characteristics of confined concrete, Mech. Cohesive-Frict. Mater.: Mech. Cohesive-Frict. Mater. 2 (3) (1997) 237–249.
[47] J.C. Lim, T. Ozbakkaloglu, Hoop strains in FRP-confined concrete columns: experimental observations, Mater. Struct. 48 (9) (2014) 2839–2854, 2014.
[48] J.-J. Zeng, Y.-C. Guo, W.-Y. Gao, J.-Z. Li, J.-H. Xie, Behavior of partially and fully FRP confined circularized square columns under axial compression, Construct. Build. Mater. 152 (2017) 319–332.
[49] J. Shayanfar, M. Rezazadeh, J.A. Barros, H. Ramezansefat, A New Dilation Model for FRP Fully/partially Confined Concrete Column under Axial Loading. The 3RD RILEM Spring Convention 2020 Ambitioning a Sustainable Future for Built Environment: Comprehensive Strategies for Unprecedented Challenges, 2020. Guimarães Portugal 2020.
[50] T. Lertsrisakulrat, K. Watanabe, M. Matsuo, J. Niwa, Experimental study on parameters in localization of concrete subjected to compression, J. Mater. Concr. Struct. Pavement 669 (50) (2001) 309–321.
[51] D.C. Candappa, J.G. Sanjayan, S. Setunge, Complete triaxial stress-strain curves of high-strength concrete, J. Mater. Civ. Eng. 13 (3) (2001) 209–215.
[52] J. Shayanfar, M. Rezazadeh, J.A. Barros, Theoretical prediction of axial response of FRP fully/partially confined circular concrete under axial loading, in: International

Conference on Fibre-Reinforced Polymer (FRP) Composites in Civil Engineering, Springer, Cham, 2021, pp. 1439–1449.
[53] G. Lin, J.G. Teng, Advanced stress-strain model for FRP-confined concrete in square columns, Compos. B Eng. 197 (2020), 108149.
[54] J. Yang, J. Wang, Z. Wang, Axial compressive behavior of partially CFRP confined seawater sea-sand concrete in circular columns–Part II: a new analysis-oriented model, Compos. Struct. 246 (2020), 112368.
[55] Carreira, Chu, Stress-strain relationship for plain concrete in compression, Journal Proceedings 82 (6) (1985) 797–804, 1985.